3D Numerical Models for Along-axis Variations in Diking at Mid-Ocean Ridges

X. Tian,[1] Eunseo Choi,[1]

Corresponding author: X. Tian, Center for Earthquake Research and Information, University of Memphis, 3892 Central Ave., Memphis, TN 38152, USA. (xtian@memphis.edu)

[1]Center for Earthquake Research and Information, University of Memphis, 3892 Central Ave., Memphis, TN 38152, USA.

Abstract.   Bathymetry reveals diverse morphologies at Mid-ocean Ridges (MORs). Previous studies show that the morphologies at slow spreading MORs are mainly controlled by the ratio (M) between rates of magma supply and plate extension. 2D models successfully explain many cross-sectional observations across the ridge axis. However, magma supply varies along the ridge and the interactions between the tectonics and magmatism at MORs are inevitably three dimensional. We investigate the consequences of this along-axis variations in diking in terms of faulting patterns and the associated structures using a 3D parallel geodynamic modeling code, SNAC. Many observed structural features are reproduced: e.g., abyssal hill, oceanic core complex (OCC), inward fault jump, mass wasting, hourglass-shaped median valley, corrugation and mullion structure. We also propose asynchronous faulting-induced tensile failure as a new possibility for explaining corrugations. $\bar{M} = 0.65$ is suggested as a boundary value for separating abyssal hills and oceanic core complexes (OCCs) formation. Previous inconsistency in the M range for OCC formation between 2D model results (M = 0.3∼0.5) and field observations (M < 0.3 or M > 0.5) is reconciled by the along-ridge coupling between different faulting regimes.

1. Introduction

1.1. Review of Literature

Geodynamic modeling as well as a variety of geological, geophysical observations and lab experiments have provided insight into the processes occurring at the mid-ocean ridges (MORs) [e.g., *Tucholke and Lin*, 1994; *Blackman et al.*, 2002; *Behn et al.*, 2006; *Behn and Ito*, 2008; *Ito and Behn*, 2008; *Baines et al.*, 2008; *Escartín et al.*, 2008; *Canales et al.*, 2008; *Dick et al.*, 2008; *Dannowski et al.*, 2010; *Olive et al.*, 2010; *Reston and Ranero*, 2011; *Reston and McDermott*, 2011]. In particular, the advent of high-resolution multi-beam bathymetric data has made it possible to discover differences in axial topography between slow and fast spreading ridges and morphological transition from the center of a ridge segment to the tip of the ridge segment.

Variations in morphologies among different MORs are mainly controlled by four factors: magma supply, tectonic strain, hydrothermal circulation and spreading rate [*Fowler*, 2004]. Among them, the spreading rate shows the strongest correlation with the ridge morphology. Slow-to-intermediate spreading ridges (half spreading rate less than 4 cm/yr) produce median valleys that are typically 10~20 km wide and 1~2 km deep (e.g., Mid-Atlantic Ridges, Figure 1). Fast-spreading ridges (half spreading rate greater than 5 cm/yr) like the East Pacific Rise have axial highs that are 10~20 km wide, 0.3~0.5 km high (Figure 2).

Slow spreading ridges exhibit along-axis variations in off-axis morphology, the width and depth of median valleys and crustal thickness. Figure 3 shows that the topographic profile near the center of the ridge segment (A-A′) is rather symmetrical and has a shorter wavelength with a median valley ~12 km wide and ~1 km deep. In constrast, the near-tip

42   profile (B-B′) is asymmetrical and has a much longer wavelength with a median valley

43   wider than 30 km and shows a greater relief (∼3 km). Gravity data of different ridge

44   segments along MAR (28∼31 °N and 33∼37 °N) suggests that the maximum along-axis

45   variation in crustal thickness ΔH_c of a single segment increases with the segment length

46   L [*Chen and Lin*, 1999] and the relationship is $\Delta H_c(\text{L}) = 0.0206\text{L}$ (Figure 4).

47   Magma supply at the MORs is mostly a passive process when no hot plume is present

48   [*Fowler*, 2004]. Driven by both vertical pressure difference and buoyancy due to horizontal

49   density difference, hot mantle rises up to fill the vacated room produced by the plate

50   separation. Decompression of the upwelling hot mantle results in partial melting. The

51   generated magma upwells to the upper crust and feeds the dikes at the ridge center.

52   The passive nature of the melting process at the MORs leads to the major difference

53   between fast and slow spreading ridges. At fast spreading ridges, magma is generated at

54   a higher rate than at slow spreading ridges. Thus, fast spreading ridges experience more

55   frequent diking, which efficiently releases stresses generated by far-field forces that drives

56   the plate motion. In contrast, diking is less frequent at slow spreading ridges and can only

57   partially release the stresses associated with plate motion. Thus, the brittle lithosphere

58   of slow-spreading ridges experiences internal deformations (e.g., tectonic processes like

59   normal faulting) when the deviatoric stress exceeds the internal strength of the lithosphere.

60   *Buck et al.* [2005] defined the ratio between the rates of dike widening and plate separa-

61   tion as $\text{M} = V_{dx}/2V_x$, where V_{dx} is the rate of horizontally opening by diking at the ridge

62   center and V_x is the half spreading rate of the MOR. According to this definition, $\text{M} =$

63   1 represents the case where dike injection is so frequent that magma supply is sufficient

64   to release all the tensional stresses from plate separation. $\text{M} = 0$ corresponds to the case

of no magma supply, in which diking does not account for any of the plate motion and therefore plates kinematics requires plates to go through internal deformations. As shown in Figure 5, an axial high forms at a fast spreading ridge (M = 1) due to buoyancy from lateral density difference across ridge axis but a median valley forms at a slow-spreading ridge (M = 0.5) due to near-axis normal faulting, which is in turn caused by the stretching of oceanic lithosphere.

Tucholke et al. [2008] expand the investigation on the role of M in mid-ocean ridge mechanics. They focus on the faulting behaviors of slow spreading ridges and find that the OCCs are most likely to form when M varies from 0.3 to 0.5. When M = 0.7 (Fig. 6), repeated diking pushes faults that have formed at the spreading center away from the ridge axis. Since the thickness of the brittle layer increases away from the ridge axis due to cooling effects, frictional and bending energy for maintaining the fault also increases. When the energy needed for maintaining an existing fault exceeds the energy for breaking a new near-axis fault, the old fault is replaced by the new one and most of the extension is accommodated by the new fault. When M = 0.3~0.5, the normal fault remains active for a long time and rotates to a low angle normal fault (detachment fault), exhuming the lower crust and mantle materials to the seafloor. When M < 0.3, most of the tension is accommodated by intra-plate deformations rather than by diking and as a result, faulting pattern is more complicated and unsteady.

1.2. Statement of Research Purpose

The M-factor formulation used in the previous 2D models [e.g., *Buck et al.*, 2005; *Tucholke et al.*, 2008] successfully explained major features found in across-ridge profiles of seafloor bathymetry. However, 2D models have limitations in studying the along-ridge

variations in morphology and faulting patterns. Magma supply at fast spreading ridges seems always sufficient for accommodating plate motions with little variations along the ridge axis. The relatively uniform topography along fast spreading ridges is considered to be consistent with the uniform abundance of the magma supply. However, along the slow spreading ridges, bathymetry, gravity anomaly and results from reflection and refraction seismology show strong correlation with variations in crustal thickness [e.g., *Lin et al.*, 1990; *Tolstoy et al.*, 1993; *Chen and Lin*, 1999; *Ryan et al.*, 2009]. Because oceanic crust is mainly formed by upwelling magma at the ridge center, variation in the thickness of the crust implies variation in magma supply. At slow spreading ridges, the degree of cooling by hydrothermal circulation, thermal structures and even local spreading rate [*Baines et al.*, 2008] also vary both along and across the ridge axis and they appear interrelated. Thus, for slow-to-intermediate spreading ridges, the interactions between tectonics and magmatism at MORs are inevitably 3D processes and 3D numerical models are desirable for investigating the factors that controls both across- and along-ridge morphology variations.

The purpose of this work is to extend the M-factor formulation originally developed for 2D models to 3D by implementing it into a 3D numerical modeling code SNAC [*Choi et al.*, 2008]. By systematically exploring the behaviors of the 3D models and comparing them with observations, we aim to better understand how the along-axis variation in diking at slow-to-intermediate mid-ocean ridges is responsible for the observed morphologies.

2. Methods

2.1. Method of approach

The numerical modeling code, SNAC (**S**tGermai**N A**nalysis of **C**ontinua), is an explicit Lagrangian finite element code that solves the force and energy balance equations for elasto-visco-plastic materials. Figure 7 shows major components of SNAC.

For each time step, strain and strain rates are updated based on the initial or previous velocity fields under the constraints from boundary conditions. A constitutive model returns updated stresses corresponding to these deformation measures. Internal forces are then calculated from the updated stresses, which is plugged into the momentum balance equation together with the body force term. Then, the damped net force divided by inertial mass yields acceleration at a node point, which is time-integrated to velocity and displacement.

A 3D domain is discretized into hexahedral elements, each of which is in turn divided into two sets of tetrahedra. This symmetric discretization prevents faulting from favoring a specific direction or "mesh grains".

Rheology for the oceanic lithosphere is assumed to be elasto-visco-plastic (EVP). When viscosity is high at low temperature, the EVP rheology implemented in SNAC essentially becomes the Mohr-Coulomb plasticity with strain weakening that can create shear bands that behave like faults. Strain softening is realized by cohesion decreasing with increasing amount of permanent (i.e., plastic) strain. We assume this relationship is linear for simplicity. It is sufficient for a full description of such a linear strain weakening to define initial and final values of cohesion and a critical plastic strain at which cohesion becomes the final value. We define the rate of strain weakening as the cohesion difference divided

128 by the critical plastic strain and use it as one of the model parameters. When temper-

129 ature is high and viscosity is low, the rheology becomes the Maxwell viscoelasticity and

130 can model creeping flow. This property of the EVP model makes it possible to set up a

131 structure with a brittle lithosphere and a ductile asthenosphere through a proper tem-

132 perature distribution. Rheological parameters are taken from previous studies that use

133 a similar rheology [e.g., *Buck et al.*, 2005; *Tucholke et al.*, 2008] or from lab experiments

134 [e.g., *Kirby and Kronenberg*, 1987].

135   For 3D diking processs, the strain $\Delta\varepsilon_{xx}$ associated with diking leads to stress changes,

136 $\Delta\sigma_{xx}$, $\Delta\sigma_{yy}$ and $\Delta\sigma_{zz}$. These stress changes due to diking are computed according to the

137 linear elastic constitutive equation $\sigma_{ij} = \lambda\varepsilon_{kk}\delta_{ij} + 2\mu\varepsilon_{ij}$.

2.2. Model Setup

138   The 3D models have a common geometry of 60 km $\times$ 20 km $\times$ 20 km in x, y and z

139 axes respectively with a resolution (Δx) of 1 km (i.e., Δx is the size of each hexahedron

140 element) (Fig. 8). The initial temperature field linearly increases from 0 °C at the top

141 surface to 240 °C at the depth of 6 km, reflecting enhanced cooling due to hydrothermal

142 circulation. Below 6 km, the temperature profile follows the instantaneous cooling of a

143 semi-infinite half-space model of moving plates [e.g., *Turcotte and Schubert*, 2002]. Two

144 sides perpendicular to the z coordinate axis are free-slip. Hydrostatic sea water pressure

145 is added on top of the seafloor. The heights of the water columns are locally determined

146 as (4000 - $h(x, z)$) m, where $h(x, z)$ is the topography at a location, (x, z). The bottom

147 boundary is free of shear stresses and is supported by normal stresses that equal to the

148 local lithostatic pressure (Winkler foundation) following *Buck et al.* [2005]. Temperature

149 is fixed at 0 °C on the top surface and at 1300 °C on the bottom surface.

150   Diking, controlled by the factor M, is assumed to occur in the middle of the doamin

151   (Fig. 8), where the lithosphere is the thinnest.

152   We adopt the linear isotropic elasticity, power-law viscosity of dry diabase [e.g., *Kirby*

153   *and Kronenberg*, 1987; *Buck et al.*, 2005] and the Mohr-Coulomb plastic model.   The

154   complete list of model parameters are given in Table 2.

155   Before running 3D models, we have run hundreds of psedudo-2D models for initial

156   setup and benchmarking with previous studies [e.g., *Buck et al.*, 2005; *Tucholke et al.*,

157   2008].   Preliminary pseudo-2D results show that the model behavior in faulting pattern

158   is sensitive to the rate of strain weakening. Two cases of strain weakening are tested in

159   the 3D models. In one case (denoted as Type 1 weakening), cohesion linearly decreases

160   from 44 MPa (denoted as C_i) to 4 MPa (C_e) for plastic strain accumulating from 0 ($\varepsilon^1_{p_i}$)

161   to 0.1 ($\varepsilon^1_{p_e}$). It has a characteristic fault slip of 150 m for pseudo-2D models and 300 m

162   for 3D models. The other case (Type 2 weakening) assumes cohesion linearly decreasing

163   from 44 MPa (C_i) to 4 MPa (C_e) for plastic strain accumulating from 0 ($\varepsilon^2_{p_i}$) to 0.33

164   ($\varepsilon^2_{p_e}$). In this case, the characteristic fault slip for pseudo-2D models is 500 m and for

165   3D models is 1 km. The characteristic fault slip is defined as $\Delta X_c = 3\Delta x \varepsilon_{p_e}$ where $3 \Delta x$

166   represents the thickness of the shear bands which is usually 2 to 4 times Δx (size of a

167   hexahedron element) [*Lavier et al.*, 2000]. When ΔX_c amount of slip takes place at the

168   fault interface, the cohesion of the material at the faulting interface decreases to C_e. In

169   this way, under the same amount of ΔX_c, models with different resolution should produce

170   the same faulting patterns.

171   Although how to estimate the M values from observations is a subject of on-going

172   research, constraints are available from a large dataset of bathymetry, gravity and seismic

173 surveys as well as geological drilling. Generally, at slow spreading ridges, magma supply

174 focuses at the center of the ridge segment and decreases towards the tip of the segment

175 [e.g., *Tolstoy et al.*, 1993; *Chen and Lin*, 1999; *Carbotte et al.*, 2015]. There is also evidence

176 for shorter wavelength of 10 to 20 km discrete focus of magma accretion along the ridge

177 axis [*Lin et al.*, 1990].

178 The numerical cost of a 3D model is non-trivial. For 2 Myr of model time, each model

179 usually runs on 192 cores for about 48 hours (i.e., around 10^4 core-hours).

180 Based on the observational constraints and computational cost, we start considering a

181 few scenarios of variations in M along the ridge axis. They are 1) three types of functional

182 forms, linear, sinusoidal and square root; 2) three ranges of M variation along the ridge

183 axis, 0.5 to 0.7, 0.5 to 0.8 and 0.2 to 0.8; and 3) two types of weakening rate, type 1 and

184 type 2.

185 While 18 models are possible, we could run 15 models with the available computational

186 resources. The complete list of the models is given in Table 1.

3. Results

3.1. Reference model

187 We consider the model with M varying linearly from 0.2 to 0.8 along the ridge axis with

188 type 1 weakening rate as the reference model and denote it as M28LinT1 following the

189 shorthand notations given in Table 1. We describe the general model behaviors in this

190 section and then provide details and mechanisms of the major structural features of the

191 model in the next section.

192 For the first 7.5 kyr (Figure 9.a), normal faults, represented by localized plastic strain,

193 begin to form near the ridge axis. Because stresses due to plate extension accummulate

194 faster at the lower M side than at the higher M side, faults first initiate at the lower M side

195 and then propagate to the higher M side. Such an asynchronous initiation of faults along

196 the ridge axis creates offset in breakaway at later stages, i.e., the breakaway at the lower

197 M side moves further away from the ridge axis than that of the higher M side (Figure 10).

198   Likewise, the model produces a median valley that widens and deepens with rates in-

199 versely proportional to the M value (i.e., rate of local magma supply) (Fig. 9a-c; Fig. 10a-

200 d).

201   By 52.5 kyr (Figure 9.b), the normal fault on the right-hand side of the ridge axis

202 remains active while the one on the left becomes inactive. The upper part of the active

203 fault plane (shown as plastic strain in the model) is exposed to the seafloor. As the active

204 fault slips, crust at the footwall bends in a clockwise rotation as is illustrated in Figure 11.

205   The active normal fault on the right rotates to a lower dip of $\sim$30 $^\circ$ at the root of the

206 fault and to $\sim$0 $^\circ$ at the exposed fault interface after about 240 kyrs (Fig. 9.c). However,

207 the normal fault at the higher M side (especially for M > 0.7) experiences less fault

208 rotation and the termination of the fault is closer to the ridge axis. The maximum relief

209 between the breakaway and the trough inside the median valley becomes larger than 1

210 km. In addition, $\sim$2 km wavelength corrugations begin to form between the breakaway

211 and termination at the lower M side (M < 0.35). We discuss the formation mechanism

212 for the corrugations in Discussion.

213   By 650 kyr (Figure 9.d), the detachment fault reaches its lowest dip angle and its termi-

214 nation stops moving away from the ridge axis. The original breakaway of this detachment

215 has already moved out of the model domain. The total fault offset at this point is greater

216 than the thickness of the crust and thus would be sufficient for exhuming the upper mantle

217 materials.

218 A new near-axis fault first appears at the center of the model domain with M ∈ (0.5,

219 0.65) and then propagates in positive z direction (Fig. 9.d,e). At this time, the initial

220 detachment fault is still active and takes up most of the extension.

221 The new near-axis normal fault at the higher M side cuts through the hanging wall of

222 the detachment fault at 880 kyr (Fig. 9.f). It coexists with the initial detachment fault

223 and begins to accommodate most of the intra-plate extension. This event is called the

224 "inward fault jump" [*Tucholke et al.*, 1998; *Dick et al.*, 2008].

225 By 910 kyr (Fig. 9.g), the inward fault jump completes in the M > 0.5 region: the

226 new high-angle fault takes up all the extension and the initial detachment fault becomes

227 completely inactive. The block that was previously a hanging wall to the detachment

228 becomes a footwall of the new fault, passively moving with the plate to the negative x-

229 axis direction. At the lower M side, the detachment is still active and the hanging wall

230 continues to move toward the positive x-axis direction (Figure 12). This dextral sense of

231 relative motions between the high and the low M side produces a region of sinistral shear

232 stress σ_{xz} (Figure 13) and eventually creates a transfer fault (Fig. 9.h). As the inward

233 jumped fault evolves, another dome ajacent to the initial OCC is produced at the higher

234 M side by 1000 kyr.

3.1.1. Constant M model M88ConT2

236 As a comparison to the varying M models, a constant M model is run. It shows similar

237 behaviors with corresponding 2D models from the previous studies and does not show

238 along-ridge variations in terms of morphology and faulting.

As shown in Figure 14, model M88ConT2 produces a $\sim$20 km wide and 1$\sim$2 km deep median valley, which is similar to the observation of the Mid-Atlantic Ridge. The width and depth of the median valley is almost constant along the ridge as contrast to the varying M models. The variation of the location of the breakaway and termination along the ridge that is mentioned in the reference model (M28LinT1) does not show up. Because the magma supply is constant along the ridge with M = 0.8, there is no stress perturbation along the ridge. Thus, the normal faults along the ridge initiate at the same time and the slipping rate of the fault is also constant along the ridge axis. The synchronized fault initiation results in no offset between breakaways and the constant sliping rate produces no along ridge axis variation in the position of the termination. In addition, neither corrugations nor mullion structures are generated. Normal faults alternate on each side of the ridge axis with a period of $\sim$10 km of plates extension and produce symmetrical shorter wavelength abyssal hills.

3.2. Main structural characteristics

We describe seven structural characteristics of the models: location of the termination, geometry of the trough, inward fault jump, fault alternation, mass wasting, hourglass-shaped median valley and corrugations and mullion structures. Since the details of these features differ among the models, they are useful for delineating and contrasting complicated model behaviors.

3.2.1. Location of termination

Location of a fault termination varies along the ridge as indicated by black dashed lines in Figure 9 and black arrows in Figure 15. The highest strain rate regions (red) in Figure 15 can be interpreted as the active detachment fault interfaces. Compared to the

261 two slices with M > 0.5, the distances between terminations and the ridge axis at the

262 lower M side (M <= 0.5) is larger and the dip angles of the detachment faults are lower.

263 For the ridge region with M > 0.5, the fault root is pushed away from the ridge axis due

264 to excessive diking while the termination is closer to the ridge axis due to lower slipping

265 rate of the fault and the asynchronous initiation of faulting along the ridge. Thus the

266 distance between the termination and the fault root is smaller at the higher M side and

267 the dip angle of the fault is higher. However, among the three slices of M <= 0.5, the

268 distances and the dip angles are similar. This is because one end of the detachment fault

269 roots at the same places along the ridge axis (intersection between the center dike and the

270 brittle-ductile transition), and for the other end, the moving rate of the termination has

271 a maximum value that is restricted by the far field extension rate V_x. Thus, the bending

272 rates of the detachment faults are similar among the three slices of M <= 0.5.

273   One thing needs to be noted is that the trough at the higher M side corresponds to the

274 terminations but detached from the terminations at the low M side (M < 0.5) as shown

275 in Figure 15.

276 **3.2.2. Geometry of trough**

277   The depressed narrow region that develops in the median valley is termed "trough".

278 The reference model showed that its shape in the bird's eye view evolves from a straight

279 line parallel to the ridge axis to a line oblique to the ridge axis (Figure 10.a-d). Initially,

280 the trough along the ridge corresponds to the termination. However, at the lower M side

281 (M < 0.5), as the normal fault rotates to a lower dip, the trough is no longer coincident

282 with the fault termination and is moving slowly to the left because the hanging wall is

283 pulled by the conjugate plate. However, the trough on the higher M side (M > 0.5) is

284 pushed away from the ridge axis [*Tucholke et al.*, 2008]. But since the trough cannot

285 bypass the termination, the trough at M = 0.8 is restricted closer to the ridge axis.

286 Together it generates the curved shape of the trough (Figure 10.d).

3.2.3. Inward fault jump

288   The inward fault jump (e.g., Fig. 9.f) occurs in most of the models when the energy

289 for maintaining an old fault becomes larger than breaking a new one near the ridge axis.

290 As shown in Figure 15, at the region with M > 0.5, the existing normal fault is pushed

291 away from the ridge-axis due to robust diking (M > 0.5). As it moves away from the

292 ridge axis, the frictional energy for the fault, the bending energy for the footwall as well

293 as the negative work done by gravity that resists the exhumation of the footwall increase

294 [*Lavier et al.*, 2000; *Olive et al.*, 2014]. The initial detachment fault remains active until

295 the sum of the negative works reaches an upper limit that breaking a new fault near the

296 ridge axis needs less work than to maintain the initial one, the initial detachment fault at

297 the higher M side is then substituted by the inward jumping fault that cuts through the

298 previous hanging wall. As the fault evolves, it connects to the initial detachment at the

299 lower M side (M < 0.5) by a transfer fault and generates a curved termination along the

300 ridge. Unlike fault alternation described below, the inward fault jump occurs on the same

301 side of the ridge axis with its along-axis extent corresponding to the M > 0.5 region.

3.2.4. Fault alternation

303   Fault alternation is the behavior that normal faults alternatively show up on each side of

304 the ridge axis when magma supply is robust enough, as shown in M88ConT2 (Figure 14).

305 The normal fault first evolves on the left-hand side of the ridge axis and produces an

306 abyssal hill parallel to the ridge axis. By 480 kyr, another normal fault evolves on the

307 other side of the ridge axis and replaces the first one. Note that among the 15 models

308 (Table 1), only three produce fault alternation. They are M88ConT2, M58SinT2 and

309 M58SqrtT2. Fault alternates only when weakening rate is low (type 2 weakening) and

310 the average integration of M along the ridge is large enough. Analysis on when and why

311 fault alternates is given in the Discussion section.

312 **3.2.5. Mass wasting**

313 Mass wasting occurs on the exposed surface of a low-angle normal fault. When the

314 weak fault zone becomes gravitationally unstable and is decoupled from the spreading

315 plate as well as the underlying material, the detached layer flows towards the lower ridge

316 axis and the lower M side driven by gravity with a velocity hundreds of times faster than

317 the half spreading rate (Figure 16; Figure 17.b,e (first row)). As the top layer of the

318 hanging wall flows down the topography slope, obvious topography drop is observed in

319 2.5 kyr (Figure 17.b versus c; d versus e (topography)).

320 Mass wasting is triggered by several factors. First, when the tip of the weak fault

321 interface moves away from the ridge axis with the spreading plate and is intersected by a

322 pre-exisitng shear stress σ_{xy} (Figure 18), the extra shear stress cuts the tip of the weak

323 fault interface and leads to the decoupling between the breakaway and the upper layer of

324 the hanging wall of the detachment fault. Second, during the roll over of the hanging wall

325 at the breakaway, tensional stress ($\sigma_{xx} > 0$) promotes the deviatoric stress for generating

326 small scale high angle normal faults cutting the detachment fault surface [*Tucholke et al.*,

327 1998] (Figure 41.c,d) and in this case the tip of the weak layer. In addition, along ridge

328 coupling tends to resist the increase in along ridge offset of breakaway which is generated

329 by along ridge varying slip rates of the faults. As Figure 19 shows, the dextral sense shear

330 stresses (red σ_{xz}) beneath the top weak layer tends to rotate the upper layer and assists

331 in triggering the decoupling process.

3.2.6. Hourglass-shaped median valley

333 All the models with M variation develop an hourglass-shaped median valley although the

334 geometry of the median valley changes with time and with the functional forms and ranges

335 of M variation. A median valley of the M28Sqrt model initially has a uniform width along

336 the ridge but is deeper on the lower M side where normal faults first form (Figure 20.a).

337 By ~100 kyr, the fault on right hand side of the ridge axis does not propagate to the

338 higher M side of the ridge and becomes inactive (Figure 20.b). It produces a depressed

339 topography curve following the inactive fault trace, which is further away from the ridge

340 axis at the lower M side but closer to ridge axis at the higher M side. On the other side

341 of the ridge axis, as the active fault rotates to a lower dip angle, breakaways at the lower

342 M side move further away from the ridge axis than the breakaways at the higher M side.

343 This along-ridge variation in the location of the breakaways act as another boundary of

344 the hourglass on the left.

345 By ~170 kyr (Figure 20.c), the hourglass-shaped median valley continues to widen and

346 deepen. Since the area of the cross section along the ridge inside the hourglass-shaped

347 median valley is approximately inversely proportional to the local M values, the shape of

348 the hourglass varies with different ranges and functional forms of M variations.

349 In addition, the further depression inside the median valley is mostly due to the elastic

350 deformation from crustal extension. As shown in Figure 21, the σ_{xx} in the median valley is

351 higher because the brittle crust is thinner, when same amount of force propagates from far

352 field extension to the median valley, the stress increases. This increased σ_{xx} is responsible

353   for the further depression and extension of the median valley on the side of the ridge axis

354   with no active faulting (Figure 20.d). For the median valley on the other side of the ridge

355   axis, mass wasting between the breakaways and the ridge axis results in further lowering

356   of topography (Figure 17.d versus e (topography)).

357   3.2.7. Corrugations and mullion structures

358   Both corrugations and mullion structures are linear structures parallel to the spreading

359   direction. As shown in Figure 9.f, at the M < 0.5 area on top of the OCC surface,

360   corrugations show a uniform wavelength of ∼2 km with hundreds of meters in amplitude.

361   At the higher M side of the ridge (Figure 9.g), a mullion structure with a wavelength of ∼7

362   km shows up on the surface of the OCC. In spite of morphological similarity, corrugations

363   and mullion structures have different formation mechanisms.

364   **Corrugations:** The corrugation starts at the breakaway as a response to tensile stress

365   in the z-axis direction. As shown in Figure 22, when the plastic strain reaches or excedes

366   0.1 (red color), on the basis of type 1 weakening, the cohesion decreases to 4 MPa. With a

367   30 ° friction angle, tensile failure is declared when the σ_{zz} reaches ∼7 MPa (yellow color).

368   The tensile stress is generated by the asynchronous faulting along the ridge. Faulting

369   initiates earlier at the lower M side of the ridge. As the fault offsets more on the lower

370   M side than on the higher M side, the footwall of the fault rotates and get uplifted more

371   on the lower M side. This relative displacement between the footwalls along the ridge

372   generates the isochron-parallel tensional stress σ_{zz}. Since σ_{zz} follows along the moving

373   tip of the plastic strain, the plastic srain together with σ_{zz} generate tensile failure that

374   propagates away from the ridge axis and thus produces the linear corrugations that are

parallel to the spreading velocity. Detailed analysis along with simpler model experiments are given in the "Discussion" section.

Mullion structures: Mullion structures observed in the models are formed by the along-ridge variation in the location of the termination due to the evolution of faulting. They usually appear where the termination is closer to the ridge axis. The shape of the footwall follows the trace of the termination as it is exhumed to the surface. Where the termination is bent inward to the ridge axis, an "initial dome" (Figure 23.a) is produced once the footwall is exhumed to the seafloor. The wavelength of the mullion structure is determined by the shape of the termination. If the pattern of the termination lasts for a long time and the footwall of the detachment fault keeps being exhumed to the surface following the trace of the detachment fault termination, a mullion structure is produced (Figure 23.b).

3.3. Effects of the functional forms of M variation

3.3.1. M28T1

Major differences among M28LinT1, M28SinT1 and M28SqrtT1 lie in the model behaviors in terms of the inward fault jump, the mass wasting and the hourglass-shaped median valley. None of the three models show fault alternation. Figure 24 shows M variations of three kinds of functional forms.

Inward fault jump: Only the linear (M28LinT1) and sinusoidal (M28SinT1) models have inward fault jump. Sqaure root model (M28Sqrt) does not have inward fault jump because during mass wasting, termination of the detachment fault retreats backward toward the ridge axis and the detachment fault is maintained near the ridge axis.

Comparing linear and sinusoidal models, timing and dimension of the inward jumping faults are different. For the linear functional form, the inward fault jump at the higher M side starts accommodating most of the extension at ∼900 kyr and replaces the initial detachment fault (Figure 25, Figure 9.f). It nucleates from the ridge center where M = 0.5 and then propagates to the M = 0.8 end with a length of ∼11 km. For the sinusoidal functional form, the inward fault jump takes the place of the initial detachment fault earlier at ∼550 kyr with a length of 14 km (Figure 25).

The timing difference between the linear and sinusoidal models is because M28SinT1 consistently has a higher M value than the M28LinT1 (Figure 24), which results in the initial detachment fault at the higher M side (M > 0.5) of M28SinT1 being pushed off axis faster than M28LinT1 and thus forming an earlier inward fault jump. The length difference is because M28SinT1 has a greater length along the ridge axis of M ≥ 0.5 (Figure 24).

Mass wasting:

Mass wasting only happens in the M28SqrtT1 model. Qualitatively, it is because M28Sqrt has a much higher value of $\frac{\partial M}{\partial Z}$ at the lower M side (Figure 26), which implies a larger along ridge shear stress σ_{xz} as well as a larger difference in σ_{xy} along the ridge that result in the decoupling between the higher and lower M sides hanging walls.

Hourglass-shaped median valley: As shown in Figure 27, differences among the three models are identified. At 160 kyr, median valley for M28SinT1 has the smallest cross-sectional (x-y) area at the higher M side (center of the ridge segment). Whereas at the lower M side, M28SqrtT1 has the smallest cross section. This is because the cross section inside the median valley is inversely proportional to the local M value along the

419 ridge. Moreover, the breakaways at the lower M sides for M28LinT1 and M28SinT1 bend

420 to parallel to the ridge axis while the breakaway for M28SqrtT1 moves further away from

421 the ridge axis. In addition, M28SinT1 has a trough inside the median valley with the

422 highest curvature. At 500 kyr, M28SinT1 has the narrowest median valley at the higher

423 M side and the high topography zone on the left-hand side of the ridge axis is the widest in

424 the z-axis direction. Integrating the topography below initial elevation (0 km) inside the

425 median valleys of the three models, M28Sin has the lowest value of integration because

426 it has the largest amount of magma supply of M > 0.5 (Figure 24). In addition, the

427 termination of the detachment fault of M28SqrtT1 has the highest curvature at the lower

428 M sides. All these model behaviors correspond to the M variation (Figure 24).

3.3.2. M58T2

430 Among M58LinT2, M58SinT2 and M58SqrtT2, the major difference lies in "fault alter-

431 nation". Except for the constant M model M88ContT2, among all the models, only the

432 models with type 2 weakening and M ranges from 0.5 to 0.8 (M58) have fault alterna-

433 tion. However, M58LinT2 does not produces alternating fault during the 1.1 Myr model

434 time. Instead, one detachment fault lasts until ∼300 kyr when the inward fault jump

435 happens at the higher M side (0.65 < M < 0.8) and replaces the initial detachment fault.

436 This provides a lower limit of $\bar{M}$ that prevents fault alternation and alows a long-lived

437 detachment fault to produce an OCC. As shown in Table 3, the lower limit is 0.6425 for

438 M58LinT2. Detailed analysis of the fault alternation is given in "Discussion".

3.4. Effects of the weakening rate

3.4.1. M57SinT1 versus M57SinT2

Initially, both models develop normal faults on both sides of the ridge axis at the lower M side. In the model with the faster weakening rate (M57SinT1), faults propagate toward the higher M side and cut through the whole crust by 25 kyr but this process completes 25 kyr later in the model with slower weakening rate (M57SinT2). By ~310 kyr, the inward fault jump appears at the higher M side (M > 0.5908) of M57SinT2 whereas at M <= 0.5908, the initial fault remains active (Figure 28.c and d). However, when the weakening is fast (M57SinT1), mass wasting happens at ~260 kyr and helps to maintain a relatively higher angle fault with a termination closer to the ridge axis. The initial fault remains and no inward fault jump forms (Figure 28.a and b). In addition, the width of median valley at the lower M side is wider for M57SinT2 than M57SinT1 (Figure 28.c, d versus a, b) because slower weakening (type 2) alows a more distributed tensional stress σ_{xx} rather than fast weakening that once a fault establishes, larger amount of the tensional stress σ_{xx} is released at the fault. The amplitude of the corrugations of M57SinT1 is larger than that of slower weakening M57SinT2. This is because faster weakening rate allows a faster decrease in the cohesion. As the cohesion reaches its minimum of 4 MPa ealier when the plastic strain accummulates to 0.1, tensile failure is easy to happen in the isochron parallel direction and produces the corrugations.

M57SinT1: For M57SinT1, by 400 kyr (Figure 29.a), two antithetic faults form at the lower M side (0.5 < M < 0.6521) accommodating part of the plate extension. This makes the termination at the lower M side retreat backward to the ridge axis. By 530 kyr, the termination at the center of the ridge segment (M = 0.6299~0.6618) moves further away from the ridge axis (Figure 29.b). This curved termination leads to a curved topography aligning with it (white curve in the second row). By 740 kyr, another antithetic fault

forms at the lower M side (Figure 29.c). It doesn't take the place of initial fault and disappear soon, however, it again releases tensional stress and helps maintain a closer to ridge axis termination at the lower M side. By 1000 kyr (Figure 29.d), an Atlantiss Massif shape OCC is produced (lower M side has a larger dome and higher M side has a smaller dome due to the along ridge termination evolution. Corrugations with wavelength varying from hundreds meters to kilometers are also produced.

M57SinT2: For M57SinT2, instead of maintaining a detachment fault like M57SinT1, it produces inward fault jump at the higher M side. By 325 kyr (Figure 30.a), an inward fault jump happens and takes the place of the initial detachment fault at the higher M side. Between 447.5 kyr (Figure 30.b) and 450 kyr (Figure 30.c), a small scale mass wasting happens and the termination recedes backward to the ridge axis. By 600 kyr, the termination at the higher M side extends further (Figure 30.d). By 885 kyr, an inward fault jump happens at the higher M side ($0.62 < M < 0.7$) (Figure 30.e). The width of the median valley at the lower M side keeps increasing due to the distributed σ_{xx} (Figure 30.a~d).

3.4.2. M58SinT1 versus M58SinT2

A major difference between M58SinT1 and M58SinT2 is that only M58SinT2 has fault alternation.

M58SinT1: During the 1 Myr extension of the model M58SinT1, 10 phases of the evolution of faulting are identified (Figure 31.a~j). Antithetic faults, inward fault jumps, mass wasting happens with a rider block, corrugations and mullion structures produced.

By 240 kyr (Figure 31.a), due to fast weakening (type 1), cohesion along the termination is low. Stress σ_{zz} takes the advantage and generates ~ 2 km wavelength corrugations

parallel to the spreading direction as the termination moves further away from the ridge axis. Between 240 kyr (Figure 31.a) and 245 kyr (Figure 31.b), a mass wasting happens at the lower M side. The termination recedes toward the ridge axis during the mass wasting. By 345 kyr (Figure 31.c), an antithetic fault forms at the lower M side (0.5 < M < 0.5469) with an inward fault jump happening at ridge segment with M $\in$ (0.5927, 0.6763) (Figure 32). 45 kyr later, the two weak zones break through and connect to each other and take the place of the initial detachment fault at the lower M side (Figure 31.d). Due to this inward fault jump, a sinistral σ_{xz} zone (blue area in the σ_{xz} panel) forms and is bounded by the termination of the inward fault jump near the ridge axis at the lower M side and the termination of the initial detachment fault at the higher M side. By 530 kyr (Figure 31.e), the termination of the inward fault jump at the lower M side evolves to a curve with its center moving further away from the ridge axis because the inward fault jump initiates at the center and the new fault starts slipping earlier. However, the lower M side of the curve remains closer to the ridge axis due to the antithetic fault and the other end of the curve is also closer to the ridge axis because the fault initiates later. This curved termination at the lower M side also connects to the initial detachment fault at the higher M side which is further away from the ridge axis. Together, the curved termination is like a mirror reflected letter "S". This flipped "S" shape termination is also shown in topography. As the curved termination at the higher M side lasts for ∼300 kyr since ∼390 kyr, following the shape, a ∼10 km in wavelength and ∼7 km in along spreading direcion mullion structure is formed (Figure 33). By ∼680 kyr, an inward fault jump hapens at the higher M side (0.7853 < M < 0.7991). It perturbs the curved shape termination and ceases the further exhumation of the mullion structure. This inward fault

jump also produces a rider block that covers the inactive detachment fault and moves off axis following the exhuming footwall of the inward jumped fault.

Between 530 kyr (Figure 31.e) and 550 kyr (Figure 31.f), another mass wasting happens at the lower M side ($0.5 < M < 0.5469$) where a slump block with a surface area of $\sim$9 km^2 flows down the topography slope into the trough. Termination recedes backward to the ridge axis. By 580 kyr, termination at the lower M side moves further away from the ridge axis due to less magma supply. Between 580 kyr and 850 kyr, due to two antithetic faults at the lower M side (M $\in$ (0.5, 0.5469) $\cup$ (0.5927, 0.6567)), the termination at the lower M side recedes and the previous mirror reflected "S" shape termination evolves to a half circle curve (Figure 31.h). The shape is also reflected in the topography. By 960 kyr (Figure 31.i)), at the ridge segment with M $\in$ (0.6763, 0.7121), another inward fault jump replaces the detachment fault away from the ridge axis and retreats the termination backward to the ridge axis forming two half circle curves with wavelengths of around half of the model domain in z-axis. A large dextral shear zone (red region $\sim$40 ° oblique to ridge axis) is seen in the σ_{xz} panel. The shear stress σ_{xz} is produced by the inward fault jump at the center of the ridge segment that previous hanging wall changes to the footwall of the inward jumped fault and generates an offset between the old hangingwall at the lower M end and the new footwall of the inward jumped fault. By 1000 kyr, due to the along ridge coupling, the inward fault jump propogates to the end of the high M side (Figure 31.j).

M58SinT2: As shown in Figure 34, a fault initiates on the left-hand side of the ridge axis (Figure 34.a). The breakaway at the lower M side moves away from the ridge axis further than that of the higher M side. It takes longer time of $\sim$100 kyr to form a

localized fault plane through the whole ridge segment due to the slower rate of weakening

(type 2). By 215 kyr (Figure 34.b), fault alternates to the conjugate plate and gradually

replaces the initial one. Corrugations are only produced at the lower M side (M $\in$ (0.5,

0.6763)). By 330 kyr, fault alternates again. Between 490 kyr (Figure 34.d) and 495 kyr

(Figure 34.e), a mass wasting happens with termination receding. A slump block with an

area of $\sim$16 km^2 flows down the topography slope into the trough. With fault alternation,

the shape of the median valley is no longer a typical hourglass. However, at the lower

M side, the median valley is still wider and deeper. Smaller wavelength abyssal hills are

produced at the higher M side.

3.4.3. M58SqrtT1 versus M58SqrtT2

The major difference between M58SqrtT1 and M58SqrtT2 is also whether the normal

fault alternates or not.

M58SqrtT1: By 260 kyr, breakaway at M = 0.5 moves $\sim$5 km further away from the

ridge axis than that at the higher M end (Figure 35.a). Corrugations with a wavelength of

$\sim$2 km are produced along the ridge. By 370 kyr (Figure 35.b), due to larger value of $\frac{\partial M}{\partial Z}$

at the lower M side, a vertical tensile failure takes place at M $\in$ (0.5, 0.5949). Two parallel

sinistral shear stress zones (blue) are seen in the σ_{xz} panel. By 400 kyr (Figure 35.c), an

inward fault jump happens where M $\in$ (0.5949, 0.7121) and it propagates to the end of the

higher M side and replaces the initial detachment fault at the higher M side by 460 kyr

(Figure 35.d). By 590 kyr (Figure 35.e), an inward fault jump happens at the lower M side

(M < 0.5949) and connect with the normal fault at the higher M side replacing the initial

detachment fault. An $\sim$18 km^2 triangular shape (bird's-eye view) rider block is produced

at the lower M side. Termination at the center of the ridge segment moves the furthest

away from the ridge axis. This is because the previous inward fault jump first initiates there and starts slipping earlier. It is also because the value of M is lower at the segment center than the higher M end. By 660 kyr (Figure 35.f), as the previous inward jumped fault at the higher M side evolves, another dome is produced. There is a hint of high angle normal fault at the region with M < 0.5949 on the conjugate plate. But it doesn't develop. By 730 kyr (Figure 35.g, the termination evolves to a "half circle" and the shape is also seen in the topography. By 780 kyr (Figure 35.h), another inward fault jump appears at the ridge segment with M $\in$ (0.6342, 0.7121) and produced a curved termination with a wavelenth of $\sim$10 km. It has the potential to create a large wavelength mullion structure. Meanwhile, at the lower M side (M < 0.5949) near the ridge axis, an antithetic fault forms and propagates toward the higher M side (Figure 35.i). It triggers another inward fault jump at the lower M side and produces another rider block. The inward jumped fault later connects with the detachment fault at the higher M side (Figure 35.j). In addition, a tensile failure shows its hint at the lower M side (M < 0.6342) of the conjugate plate.

M58SqrtT2: By 195 kyr (Figure 36.a), breakaway at the lower M side moves further away from the ridge axis. Three corrugations begin to show up due to isochron-parallel tensile failure. Median valley on the conjugate plate is wider at the lower M side because less magma supply results in larger amount of elastic depression. Between 195 kyr (Figure 36.a) and 200 kyr (Figure 36.b), mass wasting happens along the ridge and is followed by the termination retreat. By 270 kyr fault alternates (Figure 36.c). The shape of the alternated fault follows the curved shape shear σ_{xy} zone (red) as seen since $\sim$195 kyr on the left-hand side of the ridge axis. By 330 kyr (Figure 36.d), at the lower M side, an inward fault jump happens and takes the place of the old fault further away from the

ridge axis. By 460 kyr (Figure 36.e), fault alternates again to the right hand side of the

ridge axis.

3.5. Effects of the range of M variation

Generally, M57 and M58 models create a median valley much narrower and shallower

than that of M28 models.

3.5.1. SinT1

M57SinT1 versus M58SinT1: For description of M57SinT1 evolution with respect

to time, please refer to Section 3.4.1 and Figure 29. For description of M58SinT1 evolution

with respect to time, please refer to Section 3.4.2 and Figure 31. Comparing M57SinT1

and M58SinT1, the major difference is that the faulting pattern evolution for M58SinT1

is much more dynamic with a higher frequency of inward fault jumps, mass wasting

and connection of the offsetted fault zones. For M58SinT1, the inward fault jumps and

antithetic faults usually replace the old ones. However, for M57SinT1, diking is not

robust enough to create big enough stress perturbation along the ridge axis for inward

fault jumps or antithetic faults to take the place of the original one. At the lower M side,

antithetic faults only help to accommodate tensional stress which assists in maintaining

a termination near the ridge axis while the termination at the higher M side gradually

moves off axis. This produces an OCC with larger dome at the lower M side than higher

M side which is opposite to the shape of the OCC produced by M58SinT1.

M28SinT1: As shown in Figure 37, faulting evolution is much less dynamic than that

of M58SinT1. One detachment fault keeps active on the right hand side of the ridge axis.

Only inward fault jump happens ∼540 kyr (Figure 37.d). By ∼100 kyr (Figure 37.a),

breakaway at the lower M side moves ∼4 km further away from ridge axis than the higher

M side. By 250 kyr (Figure 37.b), ∼4 corrugations begin to evolve at the lower M side (M

∈ (0.2, 0.5135)). By 420 kyr, at the higher M side, a hint of inward fault jump begins to

show up. It delvelops into an inward fault jump by 540 kyr (Figure z37.d) and propagates

toward higher M side. At the lower M side (M ∈ (0.2, 0.2939)), a tensile failure takes up

part of the plate extension and helps maintain a closer to ridge axis termination than the

moving termination at the region with M ∈ (0.4724, 0.6562) (Figure 37.e). The curved

toward ridge axis termination at the lower M side produces a mullion structure.

3.5.2. M57SinT2 versus M58SinT2

For description of M57SinT2 evolution with respect to time, please refer to Section 3.4.1

and Figure 30. For description of M58SinT1 evolution with respect to time, please refer to

Section 3.4.2 and Figure 34. A major difference is that M57SinT2 has no fault alternation

while M58SinT2 has.

3.5.3. M28LinT1 versus M57LinT1

For description of M28LinT1 evolution with respect to time, please refer to Section 3.1.

M57LinT1: As shown in Figure 38, between 160 kyr (Figure 38.a) and 162.5 kyr

(Figure 38.b), a mass wasting happens. The corrugations have a relatively high amplitude.

Due to less M variation (0.2), the along ridge offset in breakaways is smaller. The median

valley almost has a constant width along the ridge. By 350 kyr (Figure 38.c), a tensile

failure happens at the region with M ∈ (0.5, 0.61) and generates a linear topography low.

Another shorter tensile failure at the higher M side (M > 0.64) helps maintain a high angle

normal fault near the ridge axis. By 430 kyr (Figure 38.d), the tensile failure at the lower

M side (M < 0.52) is responsible for the retreat of the termination. Whereas at M ∈ (0.54,

0.59), the termination moves further away from the ridge axis. This curved termination

623 results in a "dog bone" shape topography as seen at 640 kyr (Figure 38.e) and is also

624 responsible for the large sinistral shear (blue) stress σ_{xz}. By 705 kyr (Figure 38.f), an

625 inward fault jump happens and replaces the original detachment fault at the higher M side

626 with a length of ~15 km. This inward jumped fault connects with the detachment fault

627 at the lower M side. The new "L" shape termination is responsible for the topography

628 seen at 1000 kyr (Figure 38.h). The termination at the higher M side soon catches up the

629 termination at the lower M side due to the presence of a tensile failure.

4. Discussion

4.1. Overview of model behaviors

630 Model results show systematic changes with the average M value ($\bar{M}$), which is the

631 integration of M along the ridge divided by the ridge length. $\bar{M}$ values of all the models

632 are listed in Table 3. $\bar{M}_{M58} > \bar{M}_{M57} > \bar{M}_{M28}$ and within each M range, $\bar{M}$ with sqaure

633 root functional form is higher than that with sinusoidal form, which in turn is higher than

634 the linear form.

635 To facilitate the challenging task of describing the complicated behavior of each model

636 as well as comparing different models, we visualize the model behavior as shown in Fig. 39.

637 Each plot has the amount of extension in km as the horizontal axis and M values as the

638 vertical axis. The plot can succinctly show what structure appears, how long it takes to

639 be created or remains active, and where it is created along the ridge.

640 For instance, from the plot for M57SinT1 ($\bar{M} = 0.6223$) in Fig. 39, one can see that an

641 antithetic fault first shows up after about 17 km of extension on the low M end, a mass

642 wasting event occurs after about 13 km of extension and the inward fault jump is absent

in this model. Similarly, the plot for the M57SqrtT1 model ($\bar{M} = 0.6279$) clearly shows

that this model experiences two inward fault jumps.

Models with type 1 weakening, on the left column of Figure 39, show more complex

and dynamic behavior as $\bar{M}$ increases. In other words, more of the main structural

characteristics are created and they tend to have a higher recurrence frequency as $\bar{M}$

increases.

For instance, the inward fault jump occurs earlier and lasts a shorter period of time in

M28SinT1 than in M28LinT1 due to a higher $\bar{M}$ of M28SinT1. Furthermore, among three

models with M28T1, mass wasting occurs only in M28SqrtT1, the model with the highest

$\bar{M}$ among these M28T1 models. The trend of greater complexity for higher $\bar{M}$ continues

in the group of M57T1 models. Corrugations are created earlier along the whole 20 km

ridge segment than in the M28-T1 models. Unlike the M28T1 group, all three models

in the M57-T1 group have mass wasting. The two M58 models have 3 or 4 inward fault

jumps but the M57 models have at most two of them. Also, corrugations are created

earlier in the M57 models than in the M58 ones, which suggests that corrugation favors

a specific range of $\frac{\partial M}{\partial Z}$, not necessarily higher $\bar{M}$. Between M58SinT1 ($\bar{M} = 0.6834$) and

M58SqrtT1 ($\bar{M} = 0.6918$), the major difference is M58SqrtT1 has two times of inward

fault jumps at the lower M side because M values are higher at the lower M side.

When comparing models with different weakening rates, the most obvious difference is

that only type 2 models generate alternating faults. The models that exhibit the fault

alternation do not create mullion structures because the pattern of termination can not

last long enough to produce the mullion structure. Also, they have neither tensile failure

nor antithetic fault.

M58LinT2 ($\bar{M} = 0.6425$) does not show fault alternation, which suggests that not only the range of M (M58) but also the average M value along the ridge $\bar{M}$ are responsible for fault alternation. This provides an upper limit of $\bar{M} = 0.6425$ in our 3D models for producing long lasting detachment faults that can generate OCCs. Comparing M57T2 and M57T1 models show that M57T2 models generally have earlier inward fault jumps but later corrugations. For the model with constant M = 0.8 along the ridge axis, the inward fault jump and fault alternations have a period of ∼10 km of extension which is consistent with field observations. Corrugation, mullion structures, mass wasting, antithetic fault and tensile failure are not produced in constant M model M88ConT2 and it implies that varying M is necessary for producing those features.

In addition, the upper limit of $\bar{M} = 0.6425$ for allowing a long lasting detachment fault to produce an OCC in our model is consistent with the results from a near-bottom sidescan bathymetric profiler survey and sampling study of the Mid-Atlantic Ridge near 13 °N [*MacLeod et al.*, 2009]. As shown in Figrure 40, the average M value $\bar{M} = 0.63 \pm 0.05$ for the pink area where OCCs are present whereas when there is no OCC, $\bar{M} = 0.73 \pm 0.03$.

Under similar physical conditions of our model setup (e.g., thermal structure, rheology relationship, spreading velocity, weakening rate), the upper limit of $\bar{M} = 0.6425$ predicts a boundary value between two observed morphological end members for slow spreading ridges: 1) long wavelength OCCs generated by a detachment fault; 2) short wavelength abyssal hills result from symmetrical spreading of alternating high angle normal faults. Although the number of $\bar{M} = 0.6425$ is highly consistent with natural observation (e.g., [*MacLeod et al.*, 2009]), we still need more work for a comprehensive result because model

parameter such as viscosity of the underlying asthenosphere also contributes to whether fault alternates. For example, [*Allken et al.*, 2012] shows that higher value of viscosity of the ductile asthenosphere leads to better coupling between crust and mantle and promotes distributed muliple faulting rather than a focused long-lived detachment fault.

Previous 2D studies suggest that OCCs are most likely to form when M = 0.3 ∼ 0.5 [*Buck et al.*, 2005; *Tucholke et al.*, 2008]. However, conflicts exist between model prediction and observation in both the upper and lower limits. For the upper limit conflict that OCCs are observed with M > 0.5, *Olive et al.* [2010] suggest an explanation from a 2D model study that magma supplied in the ductile lower crust and upper mantle does not affect the faulting pattern and allows OCCs to be created under excessive diking. However, our 3D model results provide an alternative explanation: due to the along ridge coupling (i.e. torsion and shear), the region (M = 0.3 ∼ 0.5) along the ridge that promotes stable spreading by detachment faulting helps maintain the normal fault outside the region along the ridge. Once the detachment fault initiates along the whole ridge segment, it is very hard to modify the faulting pattern especially for a faster weakening rate (type 1). Thus, the detachemnt fault at the higher M side (M > 0.5) can still last for more than 20 km of plates separation (Figure 39.M28LinT1) before the fault alternation or inward fault jump ceases the exhuming process of the ultramafic mantle rocks. This along ridge coupling can also explain the conflict at the lower limit end when OCC is produced with observed M < 0.3 (e.g., *Dick et al.*, 2008; *Grimes et al.*, 2008; *Baines et al.*, 2008). Our 3D result suggests an extended range of M for OCCs formation than previous 2D studies (M = 0.3 ∼ 0.5) [*Buck et al.*, 2005; *Tucholke et al.*, 2008].

4.2. Comparing model results with natural observations

4.2.1. Inward fault jump

The term "inward fault jump" is first suggested in a study of geological and geophysical

data from the Mid-Atlantic Ridge [*Tucholke et al.*, 1998]. It is the end phase of a general

evolution of an OCC as is illustrated in Figure 41. In the begining of a long amagmatic

phase (Figure 41.a∼c) of seafloor spreading, a high angle normal fault cuts through the

brittle lithosphere and roots in the brittle-ductile transition (BDT) (Figure 41.a). When

the fault keeps slipping, the breakaway moves off axis and the fault begin to rotate to

a lower dip angle (Figure 41.b). Then, the exposed fault surface roll over and as the

detachment fault keeps exhuming lower crust and upper mantle rocks, it generates a dome

shape megamullion (OCC). The high angle normal faults cutting the detachment fault

surface is probably caused by the bending stresses during footwall roll over (Figure 41.c).

Then, when magma supply at the ridge center increases and pushes the detachment fault

away from the ridge axis, the OCC formation is terminated by the new fault near the

ridge axis which is termed as the "inward fault jump". As shown in the figure, initially,

the footwall of this new fault is mostly composed of crust material like basalt, however, if

this new fault can last a long period of time, it can also exhume lower ultramafic material.

In our model, most of the inward jumping faults last less than 5 km of plates extension

before the mantle material can be exhumed to the seafloor. However, the M28LinT1 model

produces an inward fault jump lasts for ∼15 km of extension (Figure 39.M28LinT1) and

produces a dome-shaped OCC ajacent to the initial one further way from the ridge axis

(Figure 9.h). This behavior might explain the brother Abel and Cain domes of the Kane

megamullion at 23 °N MAR. As shown in Figure 42, our model behavior is consistent with

the observation in terms of the breakaway and the wavelength of the domes assuming M

decreases form south to north along the ridge axis. First of all, the breakaway of the

detachment fault is further away from the ridge axis at the northern than the sourthern

end. Second, the Abel and Cain domes are larger than the Adam and Eve domes because

the inward fault jump lasts longer where M is relatively lower.

A seismic study [*Xu et al.*, 2009] showed that the Kane OCC is terminated at around

2.1 Myr ago when an eastward fault jump occured, i.e. when a new normal fault formed in

the rift valley and captured a segment of the basaltic hanging wall. The velocity structure

from their P wave tomography study verifies that the hanging wall block that is eastern

to the Cain dome has a lower velocity corresponding to basaltic rocks (Figure 43).

4.2.2. Fault alternation

For slow- to intermediate-spreading ridges, the off-axis morphologies have two end mem-

bers. One is shorter wavelength abyssal hills that are relatively symmetrical across the

ridge axis. They are usually found closer to the ridge segment center (crossection A-A′ in

Figure 44). The other is the long wavelength asymmetrically spreading OCCs (crossection

B-B′ in Figure 44). What is the mechanism for this distinct difference along the ridge?

The fault alternation behavior in our model provides a 3D perspective for answering the

question. When $\bar{M}$ is higher than 0.6425 with slower weakening rate (type 2), short wave-

length abyssal hills are generated. For example, M88ConT2 produces abyssal hills with a

∼10 km wavelength due to fault alternation (Figure 39.M88ConT2; Figure 14). Note that

the wavelength of the abysall hills in our models is consistent with the nature observation

as marked in Figure 44. While when $\bar{M} \leq 0.6425$, OCC is produced.

755   The parameters that controls fault alternation have been proposed by *Lavier et al.*

756   [2000]. *Lavier et al.* [2000] focused on the trade-off between bending forces (ΔF_b) as a

757   function of fault offset ΔX and force change due to strain weakening (ΔF_w) that is also a

758   function of ΔX. They showed that the strength weakening on the existing fault combined

759   with bending force resists further offset of the fault plays a major role in determining the

760   stress state at regions other than the active fault. Their analysis explains how higher

761   characteristic fault slip (ΔX_c) or slower strain weakening results in multiple faults rather

762   than only one fault. As ΔX increases on a fault at a spreading center, the change

763   in bending force ΔF_b increases and the strength at the fault interface decreases due to

764   weakening ΔF_w (Figure 45). If the net force change $\Delta F = \Delta F_b + \Delta F_w$ is positive, it means

765   that it becomes harder to maintain the existing fault and stress begins to accummulate at

766   other areas which eventually break another fault. ΔF_b initially increases fast with respect

767   to ΔX and then when the detachment fault surface roll over, ΔF_b reaches its peak value

768   and begins to decrease and then maintains a constant value. If the strain weakenging is

769   fast enough that the net effect force ΔF is always negative, then most of the stress will be

770   released by the existing fault and thus no conjugate or multiple faults will be generated.

771   Our model results are consistent with this analysis in that only weakening (slower

772   weakening with higher ΔX_c) produces an alternating normal fault on the conjugate plate.

4.2.3. Mass wasting

774   The mass wasting behavior in M28SqrtT1 model produces a fault scarp of $\sim$1km in

775   relief, 40km in length along isochron-parallel direction (Figure 46). It forms when the

776   detachment fault rolls over and induces bending stressses that generate the high angle

777   fault which cuts the weak detachment fault surface and decouples the spreading breakaway

778   and the highly deformed fault hanging wall. The topography at 13 °N Mid-Atlantic Ridge

779   also has a fault scarp with very similar curved geometry with ∼1km in relief. However,

780   the 1 km relief might be relfecting the model resolution of 1 km so further investigation

781   is necessaray. In addition, a magnetic anomaly study of the region by [*Smith et al.*, 2008]

782   reveals a perfect match at 13°5′N between the bathymetry and the magnetization that

783   the suspected eastward moving block corresponds to the positive magnetic anomalies that

784   is detached eastward from the youngest isochron on the American plate side of the ridge

785   axis (Figure 47). It might imply that the block at 13°5′N adjacent to the curved fault

786   scarp has a relative displacement toward the East and thus provides evidence for the mass

787   wasting behavior of the block.

788   **4.2.4. Hourglass-shaped median valley**

789   Due to the variation in diking along the ridge-axis, an hourglass-shaped median val-

790   ley is also produced in the model where the narrower center corresponds to the region

791   with higher magma supply (M=0.8). Hourglass-shaped median valleys are frequently ob-

792   served in nature along slow-to-intermediate spreading ridges like the Mid-Atlantic Ridges

793   [*Sempéré et al.*, 1993]. From an analysis of the sea beam bathymetry along the MAR

794   between 24 ° 00 ′N and 30 ° 40 ′N [*Sempéré et al.*, 1993], nine hourglass shape valleys are

795   identified. They share similar dimensional scale (∼40 km × ∼40 km) with our model. For

796   example, there is an hourglass around 22 ° 30 ′ that is 45 km long and 15 km wide (Fig-

797   ure 48). The observed width and depth of the hourglass can be used for inferring which

798   evolution stage the rift valley is in. For instance, the one shown in Figure 48 corresponds

799   to an early stage of our model because it has a relatively symmetrical and narrow shape

(Figure 20.b). In addition, the relatively small variation in the valley's width along the ridge is more corresponding to M57 and M58 models than the M28 models.

4.2.5. Mullion structure

Mullion structures are frequently observed on the surface of OCCs. For instance, the mullion structure on the surface of of the Cain dome has a wavelength of ∼3.5 km as marked in Figure 49.B∼B′. The geometry and length scale of these mullion structures bear significant visual similarity with those of our reference model, M28LinT1 (Figure 23). Model results indicate that the mullion structure mostly forms when the termination of the detachment fault has a curved shape that can last for a long period of time and the spreading-parallel mullion structure is produced following the shape of the termination. Where the termination is curved toward the ridge axis corresponds to the larger and higher part of the mullion structure. As shown in Figure 42, the spatial distribution of the mullion structure of the Cain dome is consistent with the termination that is curved inward to the ridge axis.

4.2.6. Corrugations

Corrugations are also produced in the models. For instance, the spreading-parallel corrugations with wavelength of several kilometers are produced in the model M58SinT1 (Figure 50).

As decribed in the "Results" section, the corrugations are formed due to isochron-parallel tensile failure which results from asynchronous faulting along the ridge. This mechanism is further verified by simpler 3D models.

When seeds (elements with prescribed plastic strain of 0.5) are partially added along the ridge segment for simulating the effects of asynchronous faulting where normal fault

initiates earlier at the region with initial seeds, corrugations are produced by the model (Figure 51.a).

However, when 10 km of sea water pressure is added on top of the seafloor to suppress tensile failure, no corrugation is produced (Figure 51.b). This verifies that the corrugation is related to tensile failure at the exposed fault plane.

In addition, when seeds are added along the whole ridge segment, which results in synchronous faulting, no corrugation is generated (Figure 52). This verifies that along ridge asynchronous faulting induced isochron-parallel tensional stress is necessary for creating corrugations.

As mentioned in *Smith et al.* [2014], wavelength of corrugations varies from meters to kilometers. Different scales corrugations sometimes coexist on the surface of a single OCC (e.g., *MacLeod et al.*, 2009). Although corrugation is a widely observed phenomenon, its formation mechanism is still mysterious [*Smith et al.*, 2006]. Several hypotheses are proposed. *Spencer* [1999] explains the corrugation by applying the continuous casting model which is analogical to the industrial casting process that the hot and ductile footwall of a detachment fault is continuously exhumed to the surface while being casted by the cold and brittle hanging wall. The domal shape of the corrugation is produced following the shape of the hanging wall. This hypothesis is similar to the formation mechanism of the mullion structure produced in our models. *Smith et al.* [2014] proposes another hypothesis that pre-existing offsetted faults along the ridge break through and connect to each other and form a curved termination that can produce corrugations. This is called the anastomosing behavior (e.g., *Ferrill et al.*, 1999; *Wong and Gans*, 2008) and is also produced in our models especially when inward fault jumps, antithetic faults or tensile

failures happen at only part of the ridge segment which perturbs the continuity of the termination along the ridge. In addition, *Tucholke et al.* [1998] mentioned that as oceanic lithosphere moves off axis, horizontally isochron-parallel extension is possible due to the contraction of the cooling lithosphere.

Besides these hypotheses, we proposed that the asynchronous faulting induced tensile failure due to varying M along the ridge axis as another possible formation mechanism for the relatively uniform ∼2 km corrugations. These corrugations can also be superimposed onto the surfaces of mullion structures or OCCs.

5. Conclusions

We model in 3D how M varying along a mid-ocean ridge segment can control the interactions between tectonics and magmatism and thereby produce the major bathymetric features observed on the seafloor. Six commonly observed MOR features are produced in our model which are inward fault jump, fault alternation, mass wasting, hourglass median valley, corrugation, and mullion structure. We show that, by comparing these features of the models and field observations, faulting history and spatial and temporal variation of magma supply can be inferred for a ridge segment.

Three controlling parameters are investigated. They are three ranges of M (i.e., M28, M57 and M58); three types of functional forms of M variation (i.e., linear, sinusoidal and sqaure root) as well as two types of weakening rates (i.e., faster type 1 and slower type 2). Although different structural features are generated by different functional forms and ranges of M variations along the ridge, the average M value ($\bar{M}$) along the whole ridge segment controls off-axis morphologies. When $\bar{M} > 0.6425$ with type 2 weakening, spreading occurs symmetrically and short-wavelength abyssal hills are produced. In constrast,

when $\bar{M} \leq 0.6425$, a long lasting detachment fault forms, which can exhume ultramafic rocks to the seafloor producing a domal OCC. Also, our 3D model results resolve the discrepancy between previous 2D model studies and field observations that model studies suggest OCC is produced when M varies from 0.3 to 0.5 but field observation reveals cases that OCC forms with observed M beyond both lower and upper limits. We propose a new perspective that along ridge coupling can explain why OCCs can form for M smaller than 0.3 or greater than 0.5. Finally, we propose that the asynchronous faulting can generate along-ridge tensile stresses of a large enough magnitude to cause tensile failure on the surface of the dome of an OCC, producing corrugations widely observed on the OCCs in nature.

References

Allken, V., R. S. Huismans, and C. Thieulot (2012), Factors controlling the mode of rift interaction in brittle-ductile coupled systems: A 3D numerical study, *Geochemistry, Geophysics, Geosystems*, *13*, doi:10.1029/2012GC004077.

Baines, G., M. J. Cheadle, B. E. John, and J. J. Schwartz (2008), The rate of oceanic detachment faulting at Atlantis Bank, SW Indian Ridge, *Earth and Planetary Science Letters*, *273*(1-2), 105–114, doi:10.1016/j.epsl.2008.06.013.

Behn, M., W. Buck, and I. Sacks (2006), Topographic controls on dike injection in volcanic rift zones, *Earth and Planetary Science Letters*, *246*, doi:10.1016/j.epsl.2006.04.005.

Behn, M. D., and G. Ito (2008), Magmatic and tectonic extension at mid-ocean ridges: 1. Controls on fault characteristics, *Geochemistry, Geophysics, Geosystems*, *9*, doi:

10.1029/2008GC001965.

Blackman, D., J. Karson, and D. Kelley (2002), Geology of the Atlantis Massif (Mid-Atlantic Ridge, 30 °N): Implications for the evolution of an ultramafic oceanic core complex, *Marine Geophysical Researches*.

Buck, R., L. Lavier, and A. Poliakov (2005), Modes of faulting at mid-ocean ridges., *Nature*, *434*(7034), 719–23, doi:10.1038/nature03358.

Canales, J. P., B. E. Tucholke, M. Xu, J. a. Collins, and D. L. DuBois (2008), Seismic evidence for large-scale compositional heterogeneity of oceanic core complexes, *Geochemistry, Geophysics, Geosystems*, *9*, doi:10.1029/2008GC002009.

Carbotte, S. M., D. K. Smith, M. Cannat, and E. M. Klein (2015), Tectonic and magmatic segmentation of the Global Ocean Ridge System : a synthesis of observations, *Geological Society of London*.

Chen, Y. J., and J. Lin (1999), Mechanisms for the formation of ridge-axis topography at slow-spreading ridges: A lithospheric-plate flexural model, *Geophysical Journal International*, *136*, 8–18, doi:10.1046/j.1365-246X.1999.00716.x.

Choi, E., L. Lavier, and M. Gurnis (2008), Thermomechanics of mid-ocean ridge segmentation, *Physics of the Earth and Planetary Interiors*, *171*(1-4), 374–386, doi:10.1016/j.pepi.2008.08.010.

Dannowski, A., I. Grevemeyer, C. R. Ranero, G. Ceuleneer, M. Maia, J. P. Morgan, and P. Gente (2010), Seismic structure of an oceanic core complex at the Mid-Atlantic Ridge, 22 ° 19′N, *Journal of Geophysical Research*, *115*, doi:10.1029/2009JB006943.

Dick, H. J. B., M. a. Tivey, and B. E. Tucholke (2008), Plutonic foundation of a slow-spreading ridge segment: Oceanic core complex at Kane Megamullion, 23 °30′N, 45

°20′W, *Geochemistry, Geophysics, Geosystems*, *9*, doi:10.1029/2007GC001645.

Escartín, J., D. K. Smith, J. Cann, H. Schouten, C. H. Langmuir, and S. Escrig (2008), Central role of detachment faults in accretion of slow-spreading oceanic lithosphere., *Nature*, *455*, doi:10.1038/nature07333.

Ferrill, D. A., J. A. Stamatakos, D. Sims, J. P. e. Evans, and S. H. e. Treagus (1999), Normal fault corrugation: implications for growth and seismicity of active normal faults, *Journal of Structural Geology*, *21*.

Fowler, C. M. R. (2004), *The solid earth: an introduction to global geophysics*, Cambridge University Press.

Grimes, C. B., B. E. John, M. J. Cheadle, and J. L. Wooden (2008), Protracted construction of gabbroic crust at a slow spreading ridge: Constraints from 206Pb/238U zircon ages from Atlantis Massif and IODP Hole U1309D (30 °N, MAR), *Geochemistry, Geophysics, Geosystems*, *9*, doi:10.1029/2008GC002063.

Ito, G., and M. D. Behn (2008), Magmatic and tectonic extension at mid-ocean ridges: 2. Origin of axial morphology, *Geochemistry, Geophysics, Geosystems*, *9*, doi: 10.1029/2008GC001970.

Kirby, S., and A. K. Kronenberg (1987), Rheology of the Lithosphere: Selected Topics, *Reviews of Geophysics*, *25*(6), 1219–1244.

Lavier, L. L., W. R. Buck, and A. N. B. Poliakov (2000), Factors controlling normal fault offset in an ideal brittle layer, *Journal of Geophysical Research*, *105*, doi: 10.1029/2000JB900108.

Lin, J., G. M. Purdy, H. Schouten, J.-C. Sempere, and C. Zervas (1990), Evidence from gravity data for focused magmatic accretion along the Mid-Atlantic Ridge, *Nature*, *344*,

935   627–632, doi:10.1038/344627a0.

936   MacLeod, C., R. Searle, B. Murton, J. Casey, C. Mallows, S. Unsworth, K. Achenbach,

937   and M. Harris (2009), Life cycle of oceanic core complexes, *Earth and Planetary Science*

938   *Letters*, *287*, doi:10.1016/j.epsl.2009.08.016.

939   Olive, J.-A., M. D. Behn, and B. E. Tucholke (2010), The structure of oceanic core com-

940   plexes controlled by the depth distribution of magma emplacement, *Nature Geoscience*,

941   *3*, doi:10.1038/ngeo888.

942   Olive, J.-A., M. D. Behn, and L. C. Malatesta (2014), Modes of extensional

943   faulting controlled by surface processes, *Geochemistry Geophysics Geosystems*, doi:

944   10.1002/2014GL061507.

945   Reston, T. J., and K. G. McDermott (2011), Successive detachment faults and mantle

946   unroofing at magma-poor rifted margins, *Geology*, *39*, doi:10.1130/G32428.1.

947   Reston, T. J., and C. R. Ranero (2011), The 3-D geometry of detachment faulting at mid-

948   ocean ridges, *Geochemistry, Geophysics, Geosystems*, *12*, doi:10.1029/2011GC003666.

949   Ryan, W. B. F., S. M. Carbotte, J. O. Coplan, S. O'Hara, A. Melkonian, R. Arko, R. A.

950   Weissel, V. Ferrini, A. Goodwillie, F. Nitsche, J. Bonczkowski, and R. Zemsky (2009),

951   Global multi-resolution topography synthesis, *Geochemistry, Geophysics, Geosystems*,

952   *10*, doi:10.1029/2008GC002332.

953   Sempéré, J.-C., J. Lin, H. S. Brown, H. Schouten, and G. M. Purdy (1993), Segmentation

954   and morphotectonic variations along a slow-spreading center : The Mid-Atlantic Ridge

955   (24 °00 ′ N ∼ 30 ° 40 ′ N), *Marine Geophysical Researches*, pp. 153–200.

956   Smith, D. K., J. R. Cann, and J. Escartín (2006), Widespread active detachment faulting

957   and core complex formation near 13 degrees N on the Mid-Atlantic Ridge., *Nature*, *442*,

doi:10.1038/nature04950.

Smith, D. K., J. Escartín, H. Schouten, and J. R. Cann (2008), Fault rotation and core complex formation: Significant processes in seafloor formation at slow-spreading mid-ocean ridges (Mid-Atlantic Ridge, 13 °-15 °N), *Geochemistry, Geophysics, Geosystems*, *9*, doi:10.1029/2007GC001699.

Smith, D. K., H. Schouten, H. J. B. Dick, J. R. Cann, V. Salters, H. R. Marschall, F. Ji, D. Yoerger, A. Sanfilippo, R. Parnell-turner, C. Palmiotto, A. Zheleznov, H. Bai, W. Junkin, B. Urann, S. Dick, M. Sulanowska, P. Lemmond, and S. Curry (2014), Development and evolution of detachment faulting along 50 km of the Mid-Atlantic Ridge near 16.5°N, *Geochemistry Geophysics Geosystems*, pp. 4692–4711, doi: 10.1002/2014GC005563.Received.

Spencer, J. E. (1999), Geologic continuous casting below continental and deep-sea detachment faults and at the striated extrusion of Sacsayhuaman, Peru, *Geology*, *27*, doi:10.1130/0091-7613(1999)027¡0327:GCCBCA¿2.3.CO;2.

Tolstoy, M., A. J. Harding, and J. A. Orcutt (1993), Crustal Thickness on the Mid-Atlantic Ridge: Bull's-Eye Gravity Anomalies and Focused Accretion., *Science*, *262*(October), 726–729, doi:10.1126/science.262.5134.726.

Tucholke, B. E., and J. Lin (1994), A geological model for the structure of ridge segments in slow spreading ocean crust, *Journal of Geophysical Research*, *99*, doi: 10.1029/94JB00338.

Tucholke, B. E., J. Lin, and M. C. Kleinrock (1998), Megamullions and mullion structure defining oceanic metamorphic core complexes on the Mid-Atlantic Ridge, *Journal of Geophysical Research*, *103*, doi:10.1029/98JB00167.

Table 1.   List of 3D numerical experiments.

Model	M range	Functional Form	Type of weakening	For short
1	0.2-0.8	Linear	Type 1	M28LinT1
2	0.2-0.8	Sinusoidal	Type 1	M28SinT1
3	0.2-0.8	Square Root	Type 1	M28SqrtT1
4	0.5-0.7	Linear	Type 1	M57LinT1
5	0.5-0.7	Sinusoidal	Type 1	M57SinT1
6	0.5-0.7	Square Root	Type 1	M57SqrtT1
7	0.5-0.7	Linear	Type 2	M57LinT2
8	0.5-0.7	Sinusoidal	Type 2	M57SinT2
9	0.5-0.7	Square Root	Type 2	M57SqrtT2
10	0.5-0.8	Sinusoidal	Type 1	M58SinT1
11	0.5-0.8	Square Root	Type 1	M58SqrtT1
12	0.5-0.8	Linear	Type 2	M58LinT2
13	0.5-0.8	Sinusoidal	Type 2	M58SinT2
14	0.5-0.8	Square Root	Type 2	M58SqrtT2
15	0.8-0.8	Constant	Type 2	M88ConT2

Tucholke, B. E., M. D. Behn, W. R. Buck, and J. Lin (2008), Role of melt supply in oceanic detachment faulting and formation of megamullions, *Geology*, *36*(6), 455, doi:10.1130/G24639A.1.

Turcotte, D. L., and G. Schubert (2002), *Geodynamics*, Cambridge.

Whitney, D. L., C. Teyssier, P. Rey, and W. R. Buck (2012), Continental and oceanic core complexes, *Geological Society of America Bulletin*, *125*, doi:10.1130/B30754.1.

Wong, M. S., and P. B. Gans (2008), Geologic, structural, and thermochronologic constraints on the tectonic evolution of the Sierra Mazatán core complex, Sonora, Mexico: New insights into metamorphic core complex formation, *Tectonics*, *27*, doi:10.1029/2007TC002173.

Xu, M., J. P. Canales, B. E. Tucholke, and D. L. DuBois (2009), Heterogeneous seismic velocity structure of the upper lithosphere at Kane oceanic core complex, Mid-Atlantic Ridge, *Geochemistry, Geophysics, Geosystems*, *10*, doi:10.1029/2009GC002586.

Table 2. Summary of 3D Model Parameters

Number	Variable	Description	Value	Units
1	W_{dike}	Dike width	2	km
2	D_{dike}	Dike depth	8	km
3	H	Crustal thickness at dike	6	km
4	dT/dy	Crustal thermal gradient	40	K/km
5	T_1	Temperature at lower boundary of crust	240	$°C$
6	g	Gravity acceleration	10	m/s^2
7	$demf$	Dimensionless force damping factor	0.8	N/A
8	dt	Time step	1.5768e+07	$second$
9	$topo_kappa$	Parameter for topography smoothing	0	N/A
10	$shadowDepth$	Ghost elements for parallel computing	2	N/A
11	$meshI$	Mesh number in X direction	60	N/A
12	$meshJ$	Mesh number in Y direction	20	N/A
13	$meshK$	Mesh number in Z direction	20	N/A
14	L_I	Length in X direction	60	km
15	L_J	Length in Y direction	20	km
16	L_K	Length in Z direction	20	km
17	ρ	Density	3000	kg/m^3
18	λ	Lamé's first parameter	30	GPa
19	μ	Shear modulus	30	GPa
20	$refvisc$	Reference viscosity	0.125e-17	Pa^{-n}/s
21	$activationE$	Activation Energy	276.0e+3	kJ/mol
22	vis_{min}	viscosity minimum cutoff	1.0e+18	$Pa*s$
23	vis_{max}	viscosity maximum cutoff	1.0e+27	$Pa*s$
24	$srexponent$	Power of power law in viscosity	3.05	N/A
25	$\varepsilon_{p_i}^1$	initial plastic strain for piecewise Type 1 weakening	0	N/A
26	$\varepsilon_{p_i}^2$	initial plastic strain for piecewise Type 2 weakening	0	N/A
27	$\varepsilon_{p_e}^1$	end plastic strain for piecewise Type 1 weakening	0.1	N/A
28	$\varepsilon_{p_e}^2$	end plastic strain for piecewise Type 2 weakening	0.33	N/A
29	C_i	initial Cohesion for piecewise weakening	44	MPa
30	C_e	end Cohesion for piecewise weakening	4	MPa
31	ϕ	Friction angle	30	$°$
32	$remesh_{timestep}$	Remesh when timestep reach its value	400000	N/A
33	$remesh_{length}$	Remesh when the fraction between current and initial global minimum of the ratio of the volume of a tetrahedron to one of its surface area is below 0.6	0.6	N/A
34	top_{Temp}	Surface temperature	0	$°C$
35	$bottom_{Temp}$	Bottom temperature	1300	$°C$
36	V_x	Half spreading rate	7.9e-10	m/s

Table 3. Average M values ($\bar{M}$) of the models. (The value is calculated by integrating M along the ridge axis and divided by the length (20 km) of the model domain in z-axis.)

Function \ M range	M28	M57	M58
Linear	0.4850	0.5950	0.6425
Sinusoidal	0.5668	0.6223	0.6834
Square root	0.5837	0.6279	0.6918
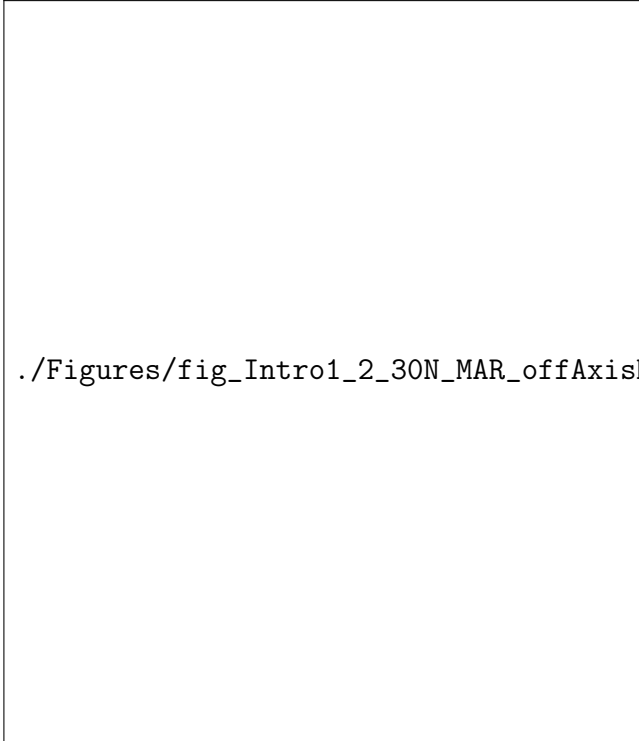
./Figures/fig_Intro1_1.eps

Figure 1. Slow spreading Mid-Atlantic Ridge

./Figures/fig_Intro1_3.eps

Figure 2. Fast spreading East Pacific Rise

./Figures/fig_Intro1_2_30N_MAR_offAxisMorphologies.eps

Figure 3. Two bathymetric profiles across the Mid-Atlantic Ridge around 30°N with vertical exaggeration of 10. A-A′ is closer to the segment center while B-B′ is at the tip of the segment.

./Figures/fig_Intro3_1.eps

Figure 4. Relationship between the maximum crustal thickness variations (ΔH_c) along a ridge segment and the segment length (L). The dashed line is the best-fit linear regression of the combined data [*Chen and Lin*, 1999].
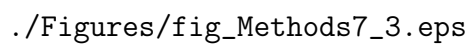
./Figures/fig_Intro5_1.eps

Figure 5.   Upper: modeling result for fast spreading agrees well with East Pacific Rise. Lower: modeling result for slow spreading ridges agrees well with the bathymetry of Mid-Atlantic Ridge. Adapted from [*Buck et al.*, 2005].
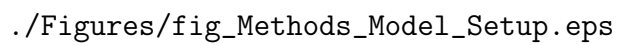
./Figures/fig_Intro_Tucholke2008.eps

Figure 6.   Snapshots of modeled fault behavior and seafloor morphology for M = 0, 0.5, and 0.7; model allows thermal evolution. Structural interpretation is superimposed on modeled distribution of strain rate; model time is indicated in panels at lower right; dashed white line at bottom is 600 °C isotherm and approximates the brittle-ductile transition; dashed seafloor is original model seafloor, red seafloor is that formed dominantly by magmatic accretion, and solid bold seafloor is fault surface. Adapted from [*Tucholke et al.*, 2008; *Whitney et al.*, 2012].
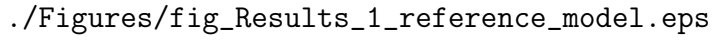
./Figures/fig_Methods7_3.eps

Figure 7. Essential components of the numerical method.

./Figures/fig_Methods_Model_Setup.eps

Figure 8. Model setup.

./Figures/fig_Results_1_reference_model.eps
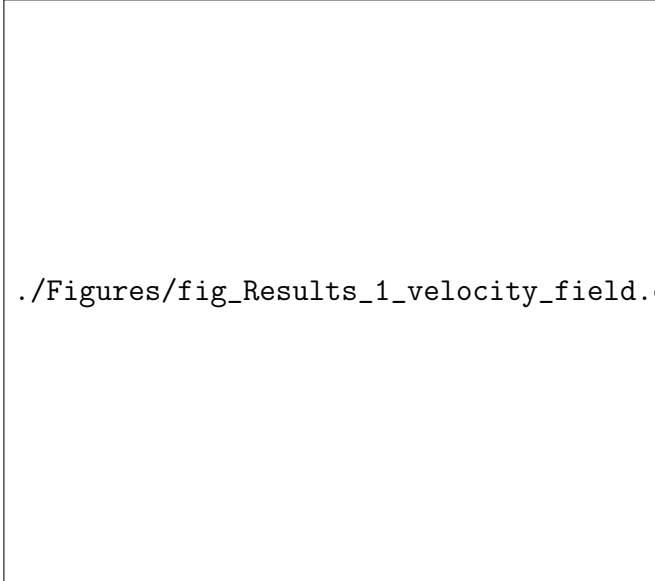
Figure 9.   Evolution of plastic strain and surface topography of the reference model M28LinT1. Each snapshot shows plastic strain plotted on the model domain, the five times vertically exaggerated topography and the time at which it is taken. The initial seafloor is at 0 km of elevation. The black dashed lines are the terminations of faults. The red dashed lines in g) and h) are the transfer faults that connect the terminations. The inset in f) plots plastic strain with opacity linearly proportional to plastic strain value.

./Figures/fig_Results1_4.eps

Figure 10.   Bird's-eye view of a breakaway in the reference model at a) 85 kyr, b) 135 kyr, c) 265 kyr and d) 295 kyr. The breakaway is marked by green solid line in a). A narrow zone of depressed topography ("trough") is marked by red dashed line inside the medain valley (blue area) in a). Color scales are the same with those in Figure 9.

./Figures/fig_Results4_8_sqrt_cut_back_bending_cartoon.eps
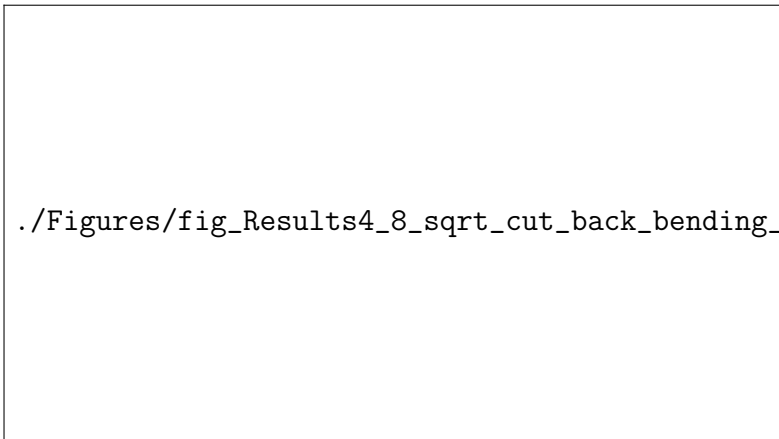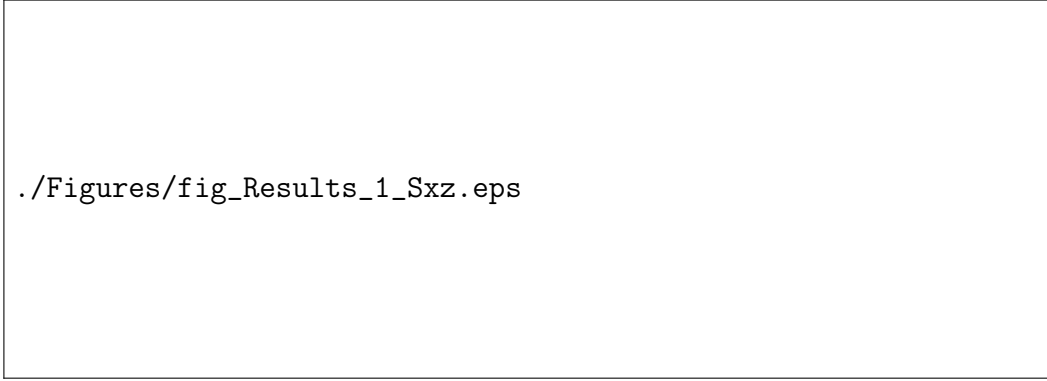
Figure 11.   Illustration of the development of bending stress in lithosphere associated with faulting at the MOR. The blue line is the neutral plane where $\sigma_{xx} = 0$. Above the neutral plane is compression ($\sigma_{xx} < 0$) and beneath it is tension ($\sigma_{xx} > 0$).
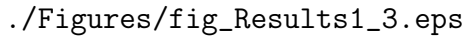
./Figures/fig_Results_1_velocity_field.eps

Figure 12. Bird's-eye view of velocity field with plastic strain ploted with opacity linearly proportional to its value. (color scale is the same as Figure 9.a))
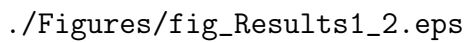
./Figures/fig_Results_1_Sxz.eps

Figure 13. Bird's-eye view of σ_{xz}.

./Figures/fig_Results1_3.eps
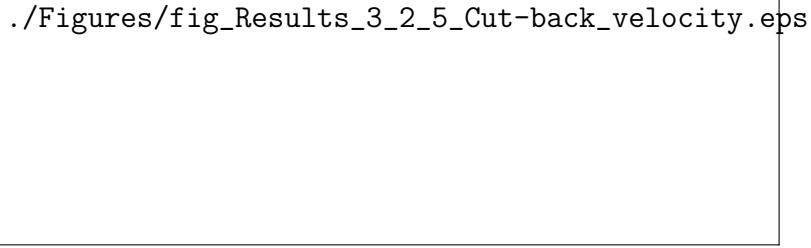
Figure 14.   Evolution of plastic strain and surface topography of the model: M88ConT2 (Table 1). Color scale of topography is the same as Figure 9.a.

./Figures/fig_Results1_2.eps
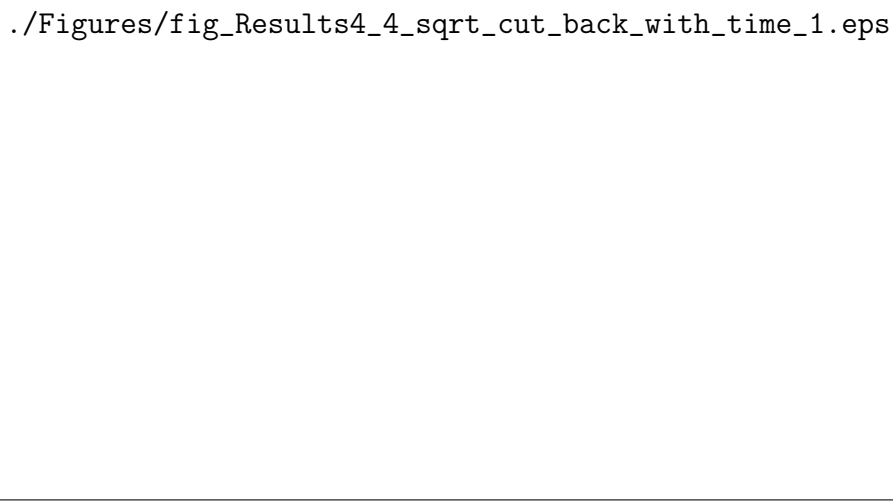
Figure 15.   The second invariant of strain rates plotted on the reference model's vertical cross sections along the ridge at 107.5 kyr. Terminations and breakaways are marked by black and red arrows.
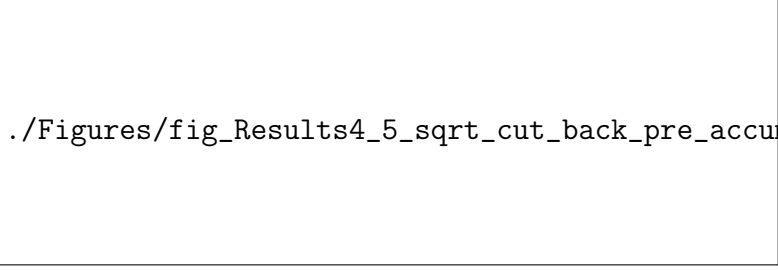
./Figures/fig_Results_3_2_5_Cut-back_velocity.eps

Figure 16.   Velocity of the mass wasting hanging wall. Magnitudes of the velocity are shown by the colors of the arrow heads. Plastic strain is plotted with opacity linearly proportional to its value.

./Figures/fig_Results4_4_sqrt_cut_back_with_time_1.eps

Figure 17.   Plastic strain, topography and stresses evolution for M28SqrtT1.
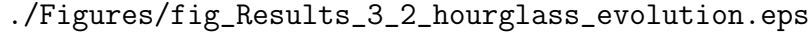
./Figures/fig_Results4_5_sqrt_cut_back_pre_accummulated_shear_zone.eps

Figure 18.   The weak detachment fault tip reaches the pre-existing shear stress. Plastic strain is plotted with opacity linearly proportional to its value.
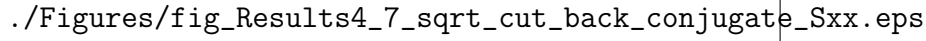
./Figures/fig_Results_3_2_5_sqrt_cut_back_Sxz_beneath.eps

Figure 19.   Along ridge axis σ_{xz} (bird's-eye view of three layers of model domain) (positive(red) means clockwise). Plastic strain is plotted with opacity linearly proportional to its value.
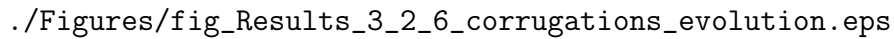
./Figures/fig_Results_3_2_hourglass_evolution.eps

Figure 20.   Bird's-eye view of the evolution of the hourglass-shaped median valley. It is generated by attaching the topography of the M28SqrtT1 model to its mirror image by assuming symmetrical M variation (0.2 to 0.8 to 0.2).
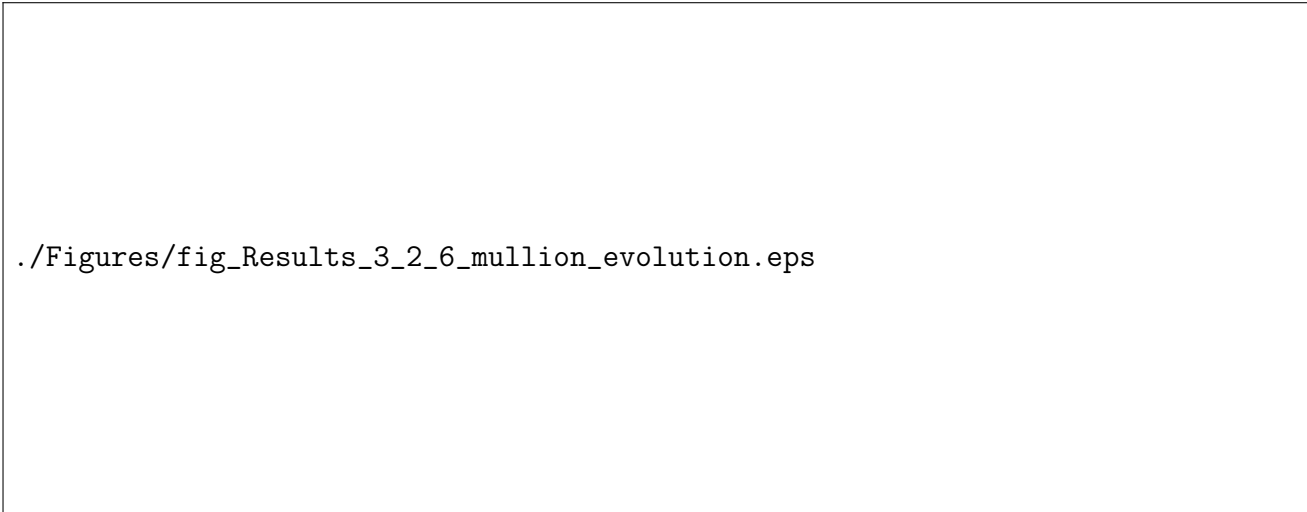
./Figures/fig_Results4_7_sqrt_cut_back_conjugate_Sxx.eps

Figure 21.   Higher σ_{xx} shows inside the median valley on the positive x-axis direction of the ridge axis.
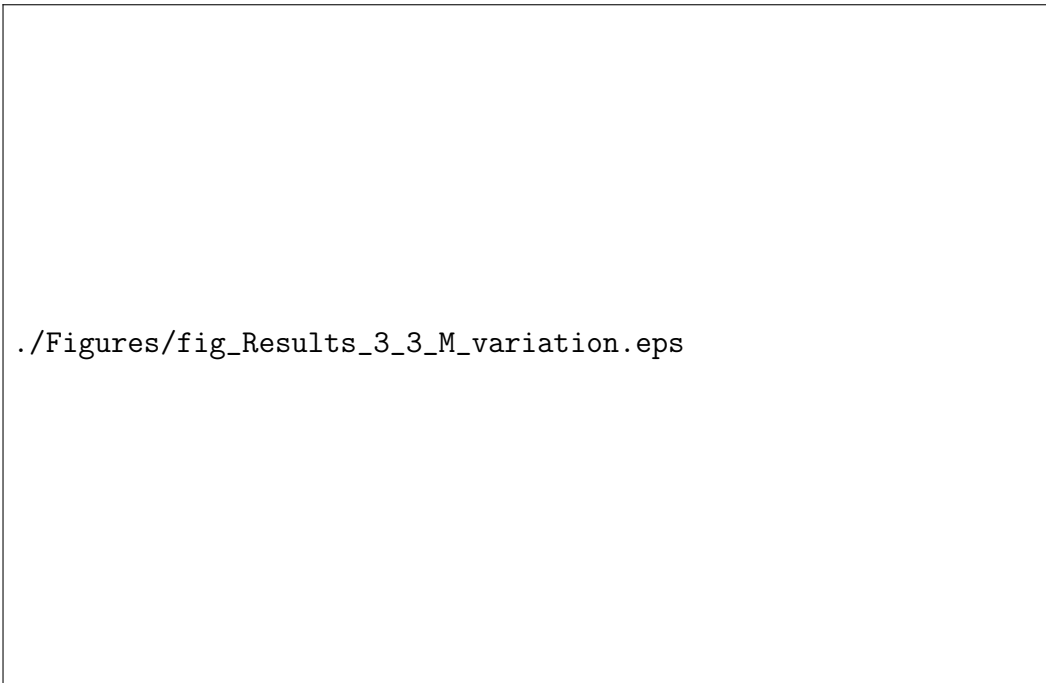
./Figures/fig_Results_3_2_6_corrugations_evolution.eps

Figure 22.   Bird's-eye view of the evolution of the corrugations. Color scales for the topography is the same as Figure 9.
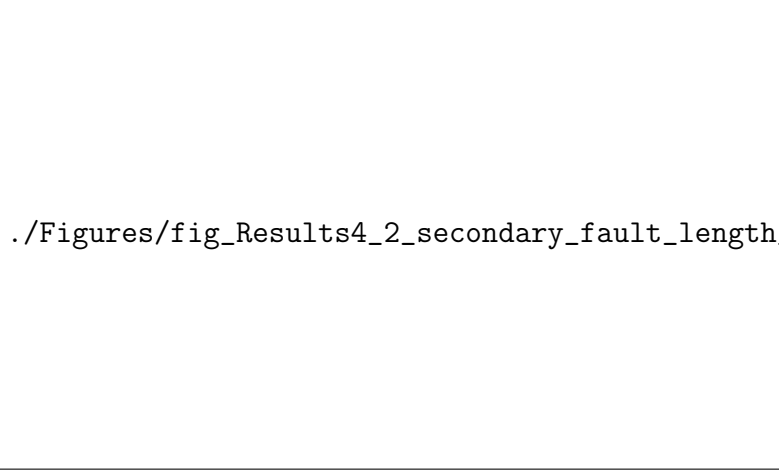
./Figures/fig_Results_3_2_6_mullion_evolution.eps

Figure 23.   Evolution of mullion structures.
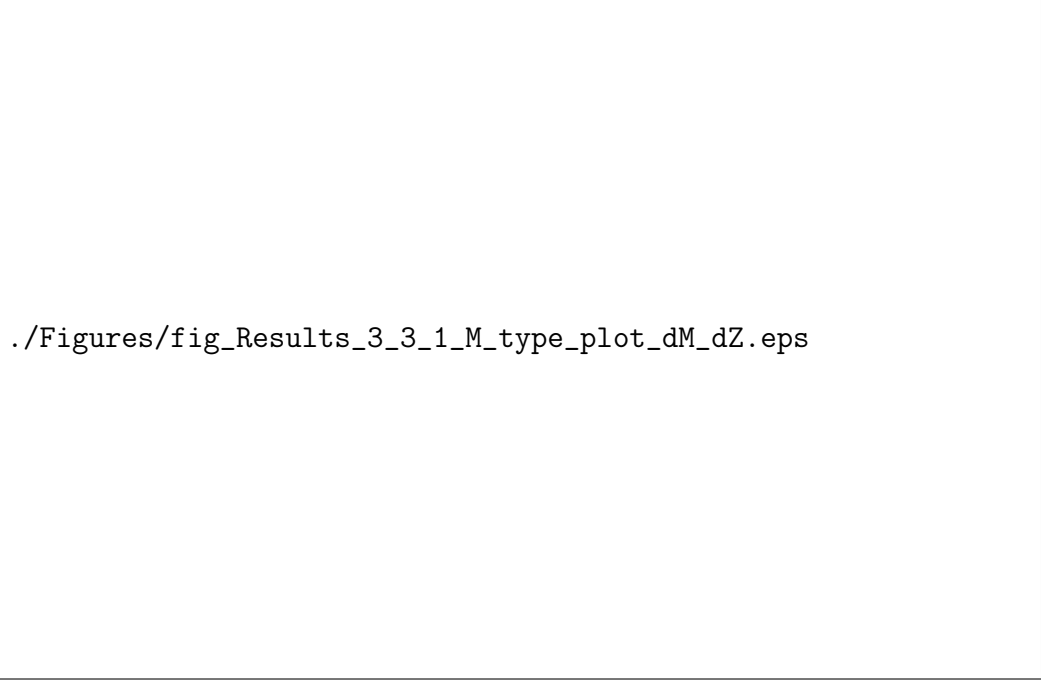
./Figures/fig_Results_3_3_M_variation.eps

Figure 24.   Three functional forms of M variation. M begins to exceed the M = 0.5 black line

at Z=10 km, 7 km, 5 km for M28LinT1, M28SinT1 and M28SqrtT1 respectively.
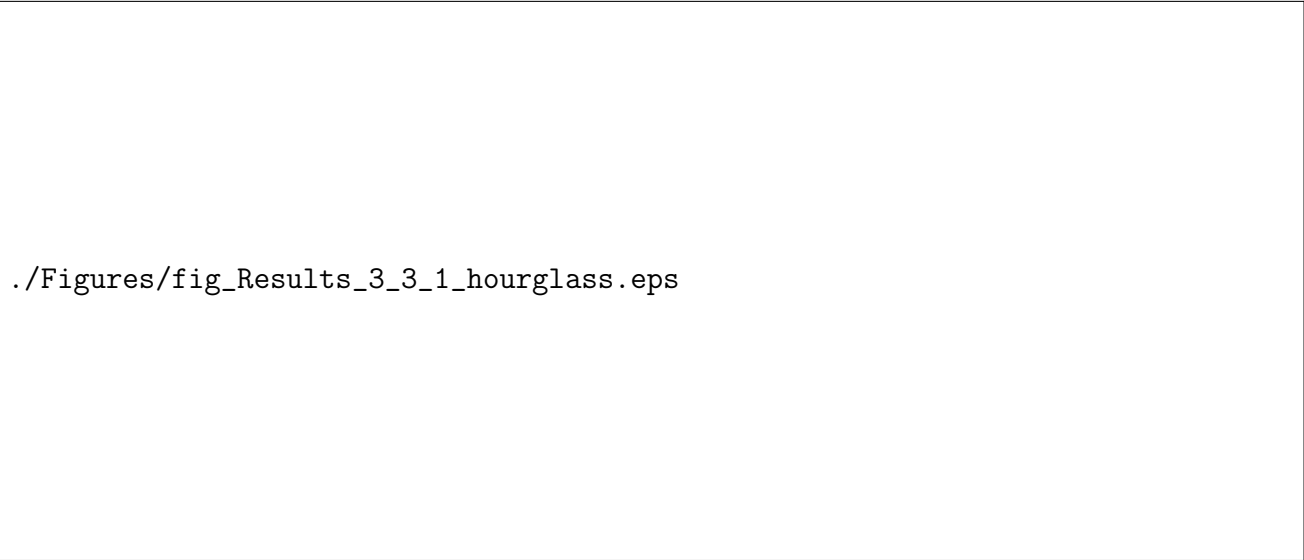
./Figures/fig_Results4_2_secondary_fault_length_comparison1.eps

Figure 25. Bird's-eye view for comparing the length and timing of inward fault jump.
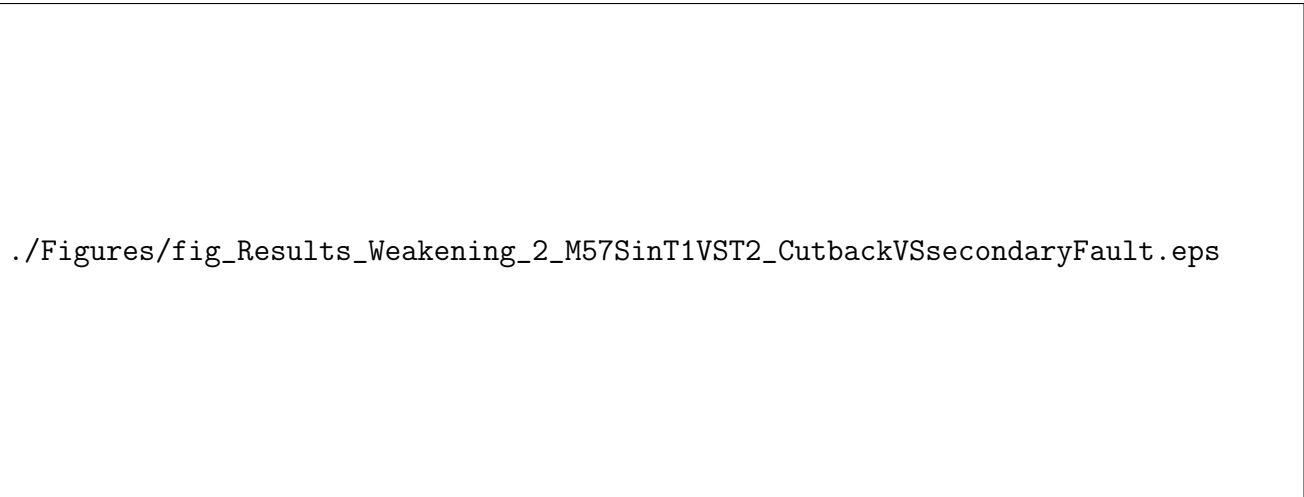
./Figures/fig_Results_3_3_1_M_type_plot_dM_dZ.eps

Figure 26. $\partial M/\partial Z$ comparision.
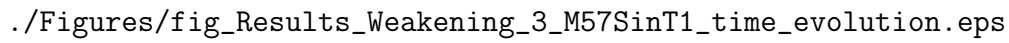
./Figures/fig_Results_3_3_1_hourglass.eps

Figure 27.   Bird's-eye view of the topograpy. (Original and mirror images are put together assumming symmetrical M variation.)
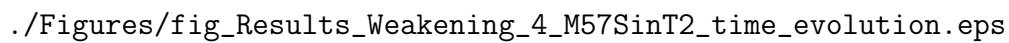
./Figures/fig_Results_Weakening_2_M57SinT1VST2_CutbackVSsecondaryFault.eps

Figure 28.   Bird's-eye view of M57SinT2 versus M57SinT1 (Table 1).
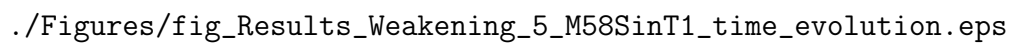
./Figures/fig_Results_Weakening_3_M57SinT1_time_evolution.eps

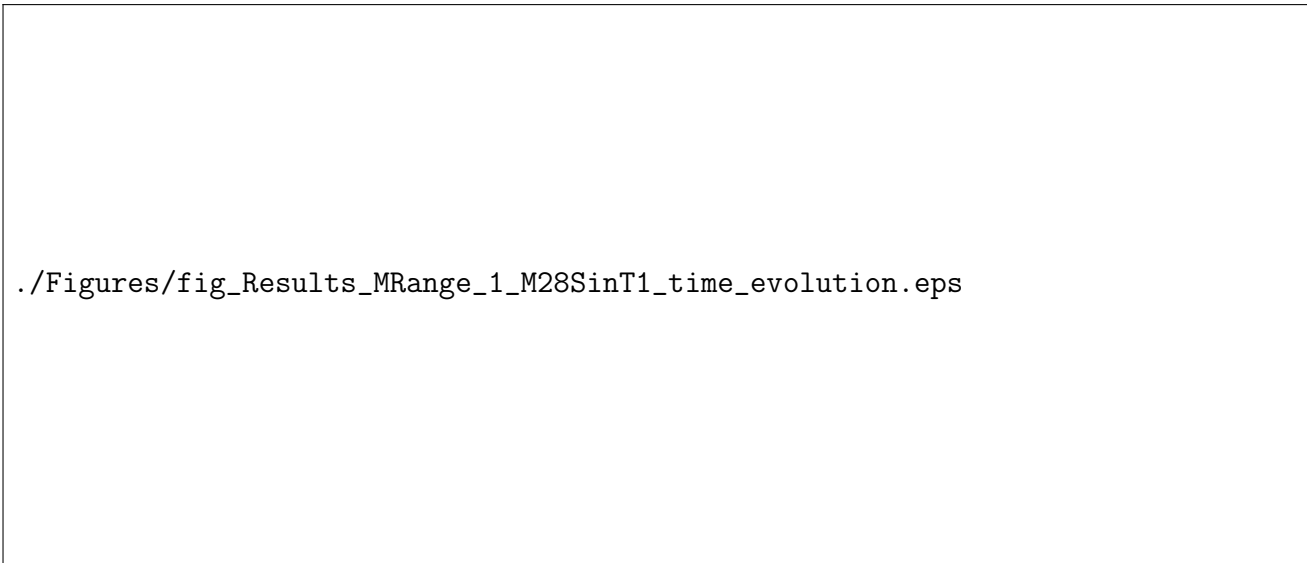**Figure 29.**   Bird's-eye view of faulting and stresses evolution of M57SinT1.

./Figures/fig_Results_Weakening_4_M57SinT2_time_evolution.eps
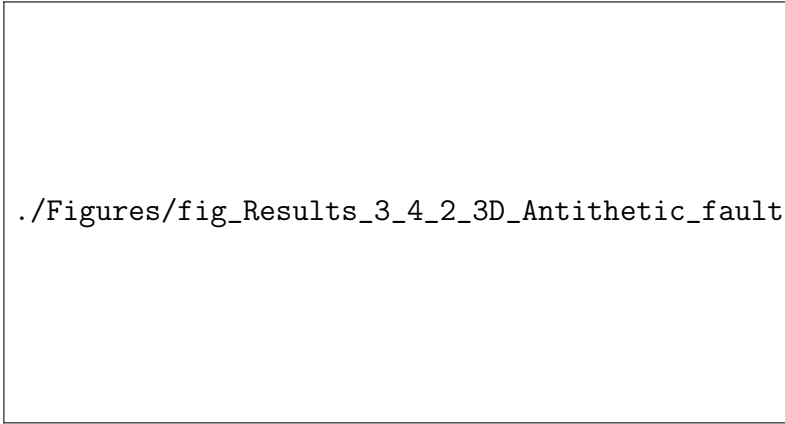
Figure 30.   Bird's-eye view of faulting and stresses evolution of M57SinT2.

./Figures/fig_Results_Weakening_5_M58SinT1_time_evolution.eps
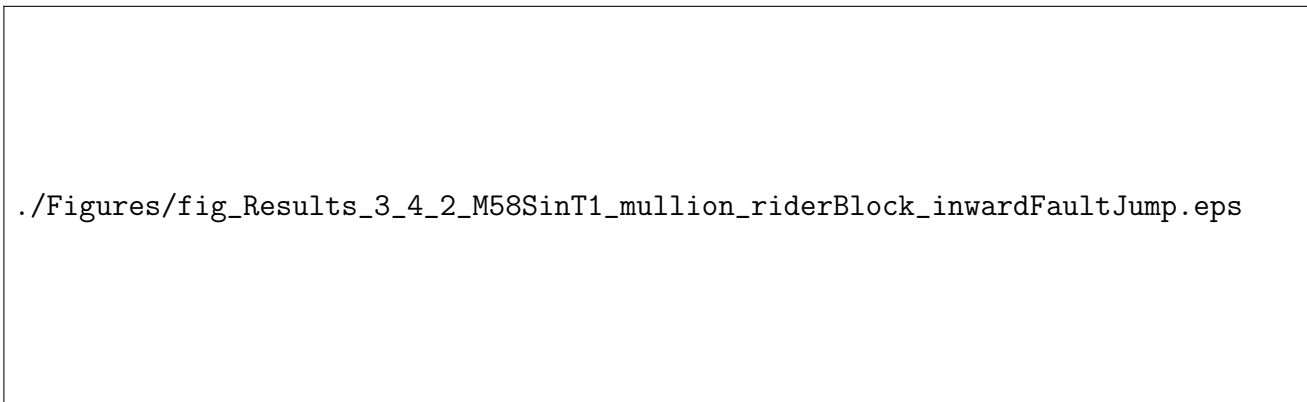
Figure 31. Bird's-eye view of faulting and stresses evolution of M58SinT1.
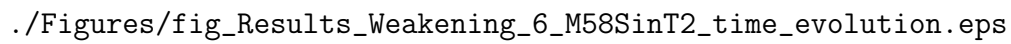
./Figures/fig_Results_3_4_2_3D_Antithetic_fault.eps

Figure 32.   Plastic strain for M58SinT1 at 350 kyr.

./Figures/fig_Results_3_4_2_M58SinT1_mullion_riderBlock_inwardFaultJump.eps

Figure 33.   Evolution of faulting and morphologies of M58SinT1.
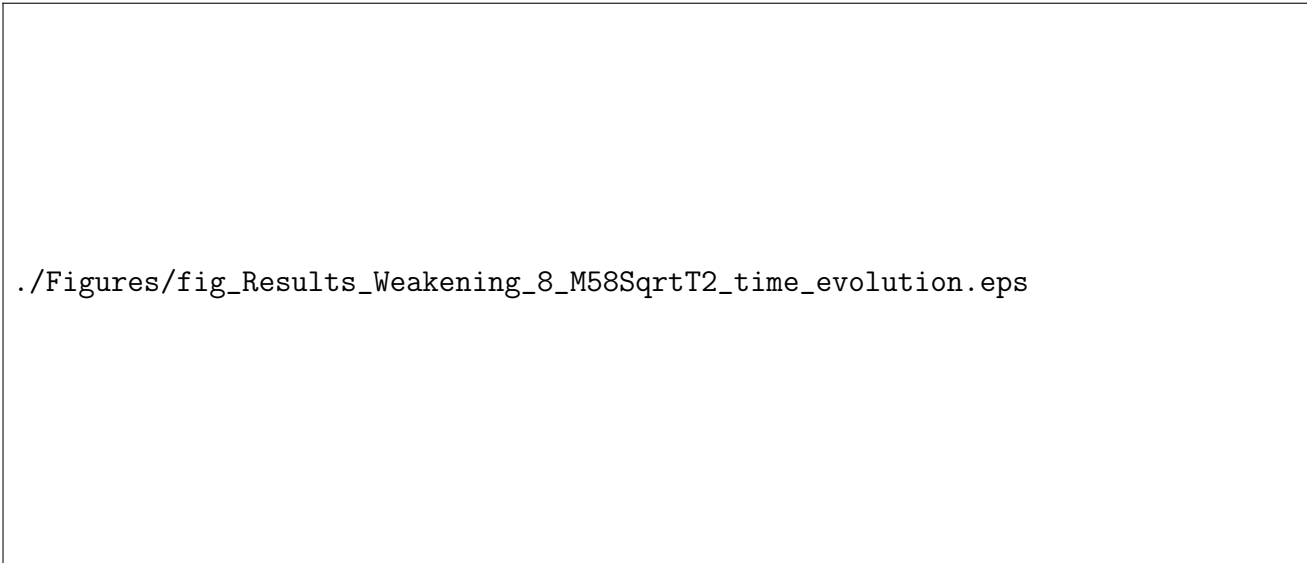
./Figures/fig_Results_Weakening_6_M58SinT2_time_evolution.eps

Figure 34. Bird's-eye view of faulting and stresses evolution of M58SinT2.

./Figures/fig_Results_Weakening_7_M58SqrtT1_time_evolution.eps

Figure 35. Bird's-eye view of faulting and stresses evolution of M58SqrtT1.

./Figures/fig_Results_Weakening_8_M58SqrtT2_time_evolution.eps

Figure 36.   Faulting and stresses evolution for M58SqrtT2.
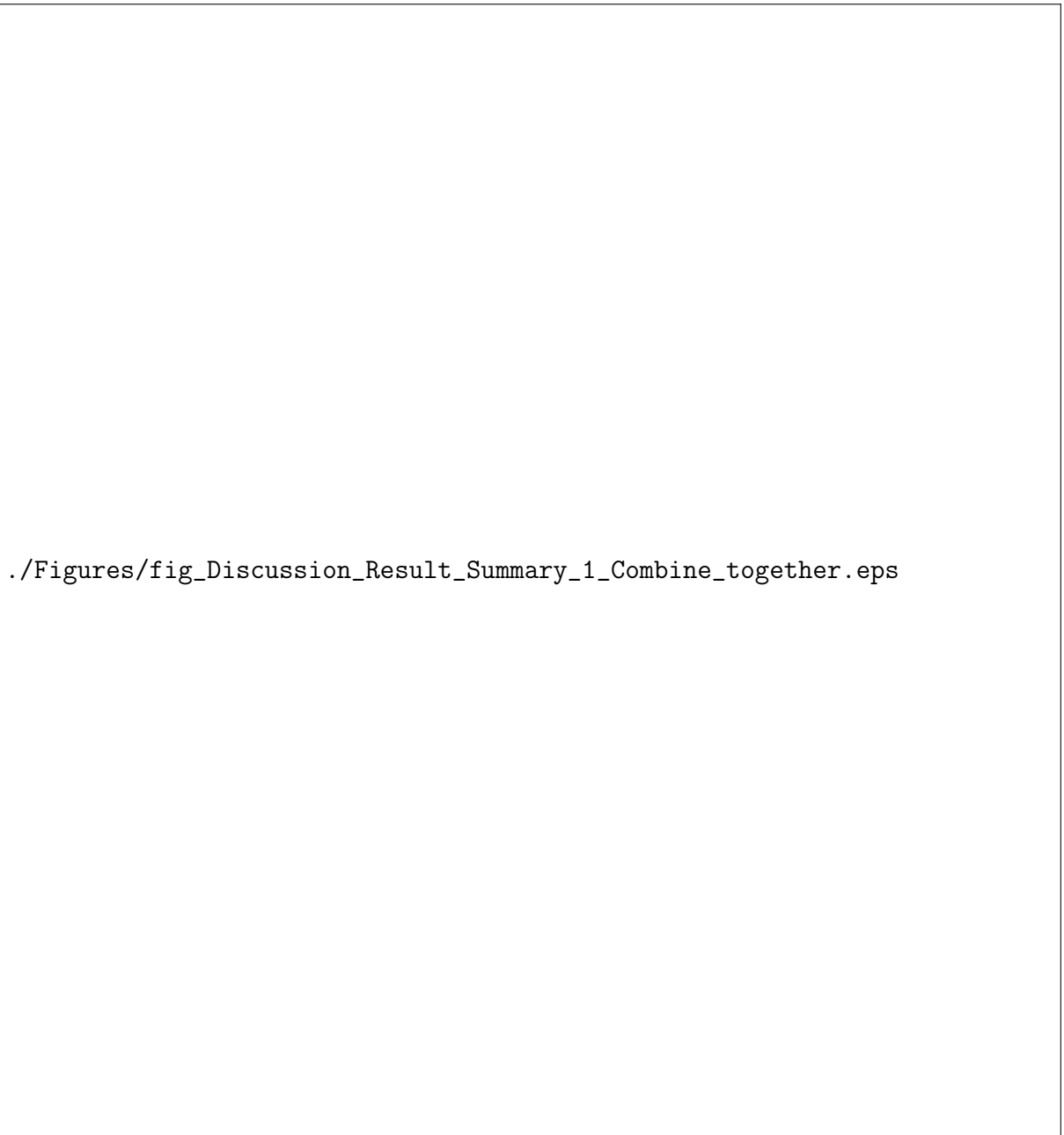
./Figures/fig_Results_MRange_1_M28SinT1_time_evolution.eps

Figure 37.   M28SinT1 (Table 1) faulting and stresses evolution with respect to time.
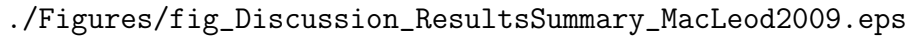
./Figures/fig_Results_MRange_2_M57LinT1_time_evolution.eps

Figure 38. M57LinT1 (Table 1) faulting and stresses evolution with respect to time.

./Figures/fig_Discussion_Result_Summary_1_Combine_together.eps

Figure 39. Initiation and duration of main structural features.

./Figures/fig_Discussion_ResultsSummary_MacLeod2009.eps

Figure 40.   Along-axis variations in total accumulated tectonic heave T in the past 1.86 Ma (since chron C2n), and consequent inferred magmatic component M (= 1 − T) as a proportion of total plate separation (blue line). Pink shaded areas delineate loci of the active or recently active OCCs. The relative contributions of tectonic strain from the western and eastern flanks of the axis that give rise to the total heave T are shown by red and green lines respectively. Adapted from [*MacLeod et al.*, 2009].

./Figures/fig_Discussion_Observation_1_Tucholke1998.eps

Figure 41.   Schematic development of a megamullion. No vertical exaggeration. (a)∼(c) shows the detachment fault evolution during amagmatic phase. (d) Increased magma supply pushed the detachment fault away from ridge axis and forms a new normal fault near the ridge axis ("inward fault jump"). Adapted from [*Tucholke et al.*, 1998].

./Figures/fig_Discussion_Observation_2_Dick2008_Kane.eps

Figure 42. Bathymetric map and simplified tectonic interpretation of Kane Megamullion. Contour interval is 100 m. Pie diagrams show lithologic proportions by weight in dredge and dive collections. Detachemtn fault breakaway and termination are marked as dashed lines. Shaded regions indicate areas of possible off-axis volcanism. Adapted from [*Dick et al.*, 2008].

./Figures/fig_Discussion_Observation_1_Xu2009_SeismicV_Kane.eps

Figure 43.   P wave isovelocity contours at 500 m below seafloor superimposed on bathymetry and simplified tectonic interpretation. Adapted from [*Xu et al.*, 2009].
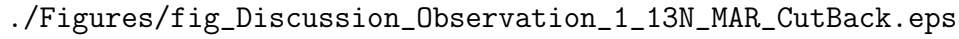
./Figures/fig_Discussion_Observation_2_13-14N_MAR.eps

Figure 44. Bathymetry from 12.8∼14.2 °N Mid-Atlantic Ridge. Crossection A∼A′ and B∼B′ are 5 times vertical exagerated. From GeoMapApp.

./Figures/fig_Results_Weakening_1_tradeOff_bend_weak.png

Figure 45.   Trade-off between change in bending force ΔF_b and weakening in the fault interface ΔF_w. H is the thickness of the brittle crust and γ is the size of initial weak perturbation and A defines the maximum bending force change. Adapted from [*Lavier et al.*, 2000]. (For more details, please refer to [*Lavier et al.*, 2000])
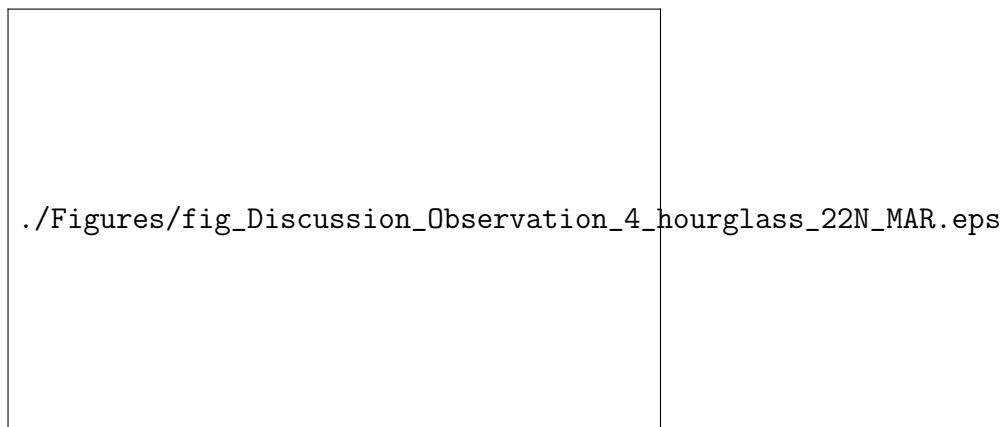
./Figures/fig_Discussion_Observation_1_13N_MAR_CutBack.eps

Figure 46. Comparing bathymetry at 13°N Mid-Atlantic Ridge to the mass wasting behavior of M28SqrtT1. The model topography is a mirror symetric flip according to the dash line, it shows the case of M varies in a square root functional form from 0.2 to 0.8 to 0.2. The bathymetry image is generated by GeoMapApp [*Ryan et al.*, 2009].

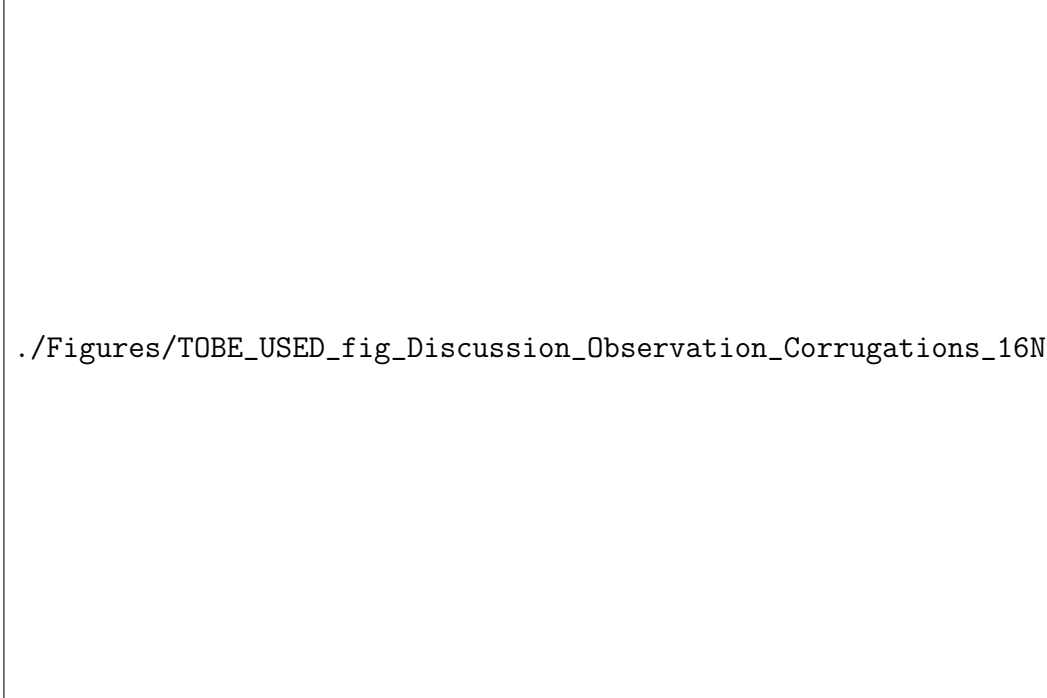./Figures/fig_Discussion_Observation_3_MassWasting_13-15N_bathymetry_magnetizaion.eps

Figure 47. Bathymetry and magnetization of 13∼15 °N MAR. Bold lines are ridge axes. Lined up circles are identified isochrons. Adapted from [*Smith et al.*, 2008].

./Figures/fig_Discussion_Observation_4_hourglass_22N_MAR.eps

Figure 48.   Hourglass median valley at 22 ° 30 ′N MAR. Image is generated from GeoMapApp.

./Figures/fig_Discussion_Observation_5_Mullion_Kane.eps

Figure 49.   Bathymetry around the Kane OCC at 23 °N MAR. Image is generated from GeoMapApp.

./Figures/TOBE_USED_fig_Discussion_Observation_Corrugations_16N_MAR.eps

Figure 50.   Comparing bathymetry at 16 °N Mid-Atlantic Ridge to the corrugations of M58SinT1 at 550 kyr.

./Figures/fig_Discussion_simple_models_for_corrugation_mechanism.eps

Figure 51.   a) Plastic strain evolution of simpler 3D model with 4 km of seawater pressure on top; b) Plastic strain evolution of simpler 3D model with 10 km of seawater pressure on top. Seeds (elements with initial plastic strain) are partially added along the ridge segment.

./Figures/fig_Discussion_Observation_6_Corrugation_simplerModel_4kwaterdepth_along_ridge_s
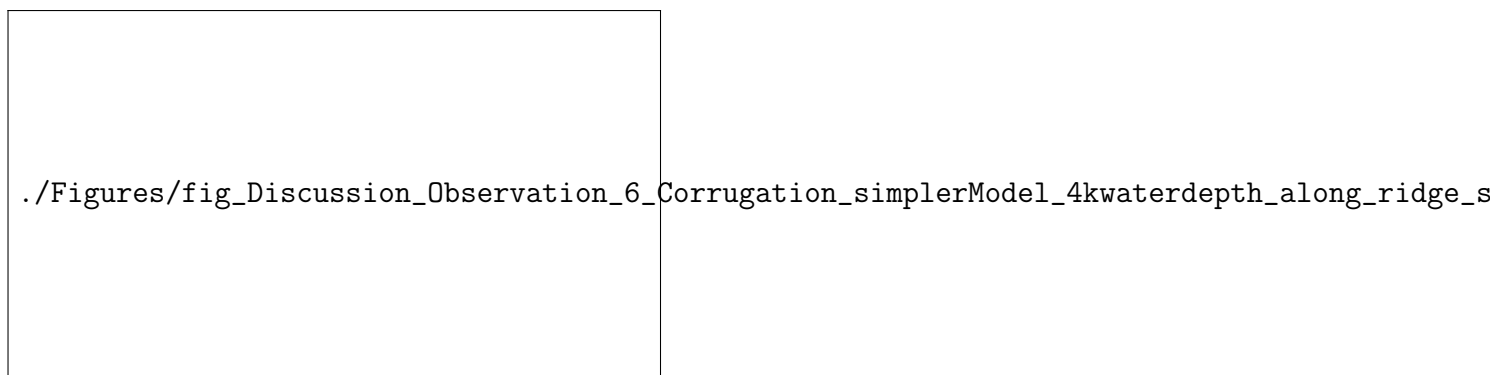
Figure 52.   Simpler 3D model with 4 km of seawater pressure on top. Seeds are added along the whole ridge segment. Color scale is the same as Figure 22.